Humboldt-Universität zu Berlin
Mathematisch-Naturwissenschaftliche Fakultät
Institut für Physik

First-principles study of α-sexithiophene polymorphs: Cohesive energies and transition paths

Masterarbeit

zur Erlangung des akademischen Grades
Master of Science (M. Sc.)

eingereicht von: Bernhard Klett

Gutachter/innen: Prof. Mag. Dr. Dr. h.c. Claudia Draxl
Prof. Dr. Stefan Kowarik

eingereicht am: March 18, 2015

Acknowledgement

During the course of this thesis I was fortunate enough to receive help from several individuals. First and foremost I would like to thank *Caterina Cocchi* for being such a great supervisor. *Pasquale Pavone* has been a source of invaluable advice on several occasions. I am grateful to *Hong Li* for helping me out with the construction of the transition path. Thank you to *Andris Gulans* for his critical reading of Chapter 3.

Abstract

Oligothiophenes present outstanding opto-electronic properties, which make them excellent candidates for a number of technological applications, ranging from thin film transistors to photovoltaic cells. Polymorphism, the ability of an element, molecule or compound to crystallize in more than one structure, is a widespread phenomenon in organic crystals and oligothiophenes in particular. It is known that both electronic and transport properties are influenced by morphologies. Therefore, an in-depth theoretical understanding of the mechanisms governing polymorphism in molecular crystals is desirable. Such an understanding is currently still missing. The focus of this work is on α-sexithiophene, which shows two stable polymorphs: a high-temperature (HT) and low-temperature (LT) phase. With the full-potential all-electron density-functional theory code `exciting`, calculations of the cohesive energies of the two polymorphs are performed. A transition path between the two polymorphs is explored, with a reaction coordinate obtained by an interpolation of the unit cell parameters, as well as the tilt and herringbone angle of the molecules. The findings allow us to estimate the energy barrier between the two phases and hence to gain insight into the microscopic mechanisms ruling polymorphism in these materials.

Contents

1 Introduction

The aim of this chapter is to provide the reader with a concise overview that will motivate the study of organic crystals and build a foundation of the physics involved. Towards this end several promising applications will be presented. Then we look at the forces acting in organic crystals and the fundamentals of polymorphism, a pervasive and important phenomenon in the study of these systems. This is followed by a review about theoretical approaches to crystal-structure prediction. Subsequently, we will introduce some of the properties of oligothiophenes, where we will particularly focus in on *sexithiophene*, which is the main subject of this thesis. Finally, we conclude with an outline of the remaining chapters.

1.1 Organic Crystals

Driven by the need for new materials with desirable properties, organic crystals have attracted a lot of interest. Organic crystalline semiconductors are promising for a variety of possible devices, ranging from organic light emitting diodes [1, 2] to organic photovoltaics [3], and organic field effect transitors [4]. The possibility of synthesizing and processing these materials at low temperature and in solution is a particularly attractive feature [5]. Organic crystals have molecules as their components, while their anorganic counterparts are built by atoms. This opens up the possibility of designing materials with predetermined properties, like the size of the band gap or charge mobilities. Of course, this requires a theoretical understanding of these systems and the capability of predicting their physical properties. Currently, this is still an open problem.

To understand organic crystals, we have to consider the forces that contribute to their cohesion. While the atoms within a molecule are held together by strong covalent bonds, the forces acting between molecules are much weaker, resulting in soft materials that often exhibit polymorphism. The intermolecular forces include interactions between permanent dipoles (Keesom force), induced dipoles (London dispersion force) or a combination thereof (Debye force). The London dispersion force is long-ranged because it varies with the distance like r^{-6}. The energies involved range from about 0.5 eV per molecule for the Keesom forces to tenths of an electron volt per molecule for London dispersion forces [5]. Most often, these forces are grouped together under the name van der Waals force. Typically, organic molecules exhibit π bonds where two atomic p orbitals form a covalent bond with another two p orbitals of a neighbouring atom. The electron-rich π system can futher interact electrostatically with another π system, giving rise to $\pi - \pi$ interaction.

1.2 Polymorphism

The weak intermolecular interactions in organic crystals allow for the molecules to crystallize in more than one structure - a phenomenon called *polymorphism*. There are two types of polymorphism in organic crystals. One type results if the molecules adopt different shapes, thereby giving rise to *conformational polymorphism*. This can occur because of torsion about a single bond, where the energies involved are of the order of $\mathcal{O}(0.05)$ eV per molecule [5], which is typically comparable to the difference in energy between polymorphs. In this work we focus on the other type, called *packing polymorphism*, which comes about as a result of different molecular arrangements. The resulting structure depends largely on the thermodynamic conditions of the synthesis. Even a few degrees of variation in the temperature can already be enough to cross the small energy barrier between polymorphs. This suggests that many materials might have polymorphs that have not yet been discovered.

The relative phase stability of polymorphs is governed by their free energies. The polymorphs with the lowest free energy will be the most stable. In crystals the differences in volume between polymorphs is small relative to the total volume and therefore changes in volume and pressure with respect to energy are considered negligible. Under these conditions the polymorphs are described in terms of the Helmholtz free energy A

$$A(T, V) = U - TS, \tag{1.1}$$

with temperature T, volume V, internal energy U and entropy S. At $T = 0$ K the most stable polymorph will have the lowest internal energy, as well as the lowest Helmholtz free energy. For higher temperatures differences in entropy have to be taken into account. Thus, the relative phase stability between polymorphs will generally be temperature-dependent. If the free energies intersect at a temperature below the respective melting points the polymorphs can undergo a reversible phase transition and are said to be *enantiotropic*. On the other hand, if the free energy curves do not intersect before one structure begins to melt the polymorphs are *monotropic*. Under these conditions one structure transforms irreversibly into the other.

1.3 Predicting Crystal Structures

A lot of research has gone into the field of crystal structure prediction [6, 7]. The problem remains difficult, even though progress is being made. Here, we will present a brief overview of the state of the art.

A computational method that is capable of reliably predicting how molecules crystallize would give us knowledge of the solid-state properties of these molecules before synthesizing them. Ideally, it would be desirable if such a method accomplishes three main tasks. First, come up with a set of hypothetical polymorphs. Second, rank the polymorphs according to their stability at a given temperature. Third, predict which

conditions will cause a certain crystal structure to grow. However, the prediction of crystal structures given just the chemical formula and the crystallization conditions has proven difficult. In Ref. [8], Gavezzotti poses the question "*Are Crystal Structures Predictable?*" and answers succinctly "No". He names the small energy differences between crystal structure candidates as primary obstacle. The Cambridge Crystallographic Data Centre has organized a series of thus far five blind tests, in which participants are asked to predict the crystal structures of organic compounds with known, but unpublished crystal structures. The latest blind test concluded that methods such as dispersion-corrected density-functional theory are now able to make reliable predictions, while standard force fields perform badly [7]. However, it must be said that crystal prediction is still an open problem, partly because only a limited (but expanding) group of molecules has been tested and partly because of the high computational cost.

1.4 Oligothiophenes

Oligothiophenes represent a well-known family of organic molecules. They consist of carbon, hydrogen and sulfur, which are arranged in a chain of thiophene rings. As the prefix *oligo* implies, the number of thiophene rings ranges from 2-8. Oligothiophenes are abbreviated as n-T, where n is the number of rings.

The crystal structures of oligothiophenes share a number of similarities. So far, all of the observed crystals show a monoclinic unit cell, with space group $P2_1/a$, $P2_1/c$, or $P2_1/n$, depending on the length of the molecule. This means the structures have a *primitive* unit cell with a twofold screw axis, that includes a translation by half the length of the respective lattice vector. Furthermore, there is a glide plane with a translation along half the **a** or **c** lattice vector, or along half a face diagonal in the case of $P2_1/n$. The repulsion between π-orbitals causes the oligothiophenes to arrange in a herringbone structure (see Fig. 6.2a). The optical properties, one of the primary reasons for the interest in these molecules, are influenced by the overlap between π orbitals. To maximize the overlap, the thiophene rings have to lie in one plane, i.e. the molecule is *coplanar*. This chemical structure is denoted by the greek letter α, as in α-6T. All of the oligothiophenes exhibit this structure with a torsion angle between rings of less than 1°. Only α-3T shows a deviation of $6° - 9°$ [9]. If the rings are twisted with respect to each other, this is called β-isomer. The number of coplanar rings determines the conjugation length. Longer conjugation lengths result in a lower splitting between adjacent energy levels. This has implications for the absorption wavelength.

1.5 Sexithiophene

Among organic semiconductors α-sexithiophene (α-6T) has shown great promise. In 1989 thin films of α-6T were used as p-type semiconductor in organic field-effect transitors. At the time charge carrier mobilities were measured in the range of $\mu = 10^{-3} - 10^{-4}$ cm^2/Vs, while the mobilities in polythiophene-based OFETs were one to two orders of magnitude

lower [10]. More recently hole-mobilites up to $\mu = 0.04$ cm^2/Vs and $\mu = 0.16$ cm^2/Vs have been realized in thin films and single crystals, respectively [11]. This suggests that the charge transport occurs mainly through channels of α-6T molecules, which are standing upright on the substrate in a herringbone structure, like in single crystals.

Sexithiophene has been observed to grow in two possible crystal structures, which are referred to as *high-* and *low-temperature* (HT and LT) [12, 13]. Both phases have a herringbone structure, with either two (HT) or four (LT) molecules per unit cell (see Fig. 1.2 and Tab. 1.1).

	6T-HT [12]	6T-LT [13]
a [Å]	9.14	44.70
b [Å]	5.68	7.85
c [Å]	20.67	6.03
β [°]	97.78	90.8
τ [°]	55	66
ϕ [°]	41.5	23.5

Figure 1.1: Unit cell parameters of the HT and the reduced LT (LTr) phase. Both phases have a monoclinic angle β. τ is the herringbone angle and ϕ is the tilt angle of the long molecule axis with respect to the a axis.

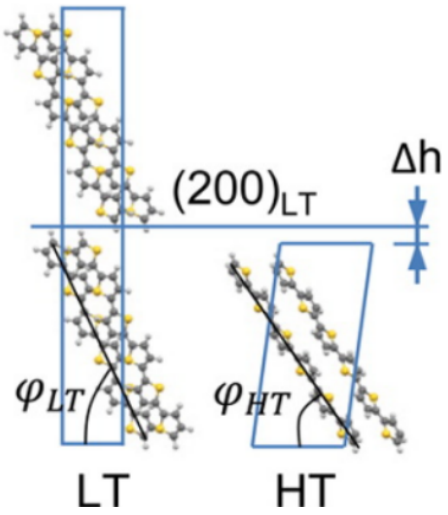

Figure 1.2: Low-temperature (LT) and high-temperature (HT) phase of 6T. The unit cell consists of four (LT) and two (HT) molecules, respectively. φ is the tilt angle. Taken from Ref. [14].

Theoretical work by Della Valle *et al.* [15] suggests the existence of thousands of distinct

energy minima. Nine of these minima are particularly deep and exhibit very different structures. Almost all of the deepest minima have a monoclinic unit cell and in all cases the number of molecules per unit cell is either 2 or 4. The two deepest minima have been identified as the HT and LT phases.

1.6 Outline

Two chapters present the theoretical foundation needed for this work. The basics of DFT are presented in Chapter 2, while Chapter 3 discusses the relevant information regarding the numerical methods. Chapter 4 covers the preparatory steps and adresses the question of numerical accuracy. The relative phase stability of the experimental structures constitutes the first part of the results and is presented in Chapter 5. Subsequently, the transition path is the topic of Chapter 6, which presents the general concepts and details how the path was constructed. The results concerning the transition barrier are presented in Chapter 7. Finally, conclusions and an outlook are given in Chapter 8.

2 Density Functional Theory

This chapter introduces the reader to *density functional theory* (DFT), a powerful computational method for investigating the electronic structure of many-body systems. After outlining the basic idea of DFT, we cover the *Hohenberg-Kohn theorem* upon which DFT is formally built. The *Kohn-Sham equations* show how a many-body system can be mapped onto to a Schrödinger equation of non-interacting particles, thus making the computation tractable. Following an overview of the different categories of exchange-correlation (XC) functionals of DFT, we focus in detail on the *local-density approximation*, which is exclusively used in this work.

2.1 Introduction to Density Functional Theory

The materials of our everyday world are made up of electrons and nuclei which are subject to electrostatic or Coulombic interaction. When investigating the electronic properties of a system, the basic problem is to solve the Schrödinger equation for the Hamiltonian describing a system of interacting electrons and nuclei. In atomic units ($\hbar = m_e = e = a_0 = 1$), which will be used throughout this thesis, the Hamiltonian is written as:

$$\mathcal{H} = -\sum_i \frac{\Delta_i}{2} - \sum_\alpha \frac{\Delta_\alpha}{2M_\alpha} + \frac{1}{2}\sum_{i\neq j} \frac{1}{|\mathbf{r}_i - \mathbf{r}_j|} - \sum_{i,\alpha} \frac{Z_\alpha}{|\mathbf{r}_i - \mathbf{R}_\alpha|} + \frac{1}{2}\sum_{\alpha\neq\beta} \frac{1}{|\mathbf{R}_\alpha - \mathbf{R}_\beta|}. \quad (2.1)$$

Here, Δ is the Laplace operator. M_α, Z_α and $\mathbf{R}_\alpha$ refer to the mass, charge, and coordinates of nucleus α. $\mathbf{r}_i$ gives the coordinates of the i^{th} electron.

The mass of a nucleus is several orders of magnitude larger than the mass of an electron (e.g. hydrogen atom $M_H \approx 1837$) Consequently, electrons are much faster than nuclei and thus operate on a shorter timescale. This allows for the separation of the motion of electrons and nuclei. The electronic motion can be described with a background potential given by the nuclei, while the nuclei in turn are subject to a potential given by electrons that adjust their positions instantaneously. This is known as the Born-Oppenheimer approximation and it is commonly used in solid state physics as well as in quantum chemistry.

The Hamiltonian for a system of N electrons in an external potential, given by the nuclei, has the form

$$\begin{aligned} \hat{H} &= \hat{T} + \hat{U} + \hat{V} \\ &= \sum_{i=1}^{N} -\frac{\Delta_i}{2} + \frac{1}{2}\sum_{i\neq j}^{N} \frac{1}{|\mathbf{r}_i - \mathbf{r}_j|} - \sum_{i,\alpha} \frac{Z_\alpha}{|\mathbf{r}_i - \mathbf{R}_\alpha|}. \end{aligned} \tag{2.2}$$

$\hat{T}$ is the kinetic energy operator. $\hat{U}$ and $\hat{V}$ refer to the electron-electron repulsion and electron-nucleus attraction, respectively. $\hat{V}$ is the *external* potential.

In principle, one only has to solve the resulting $3N$-dimensional Schrödinger equation $\hat{H}\psi(\mathbf{r}_1, ..., \mathbf{r}_N) = E\psi(\mathbf{r}_1, ..., \mathbf{r}_N)$. This does not work in a solid were we have on the order of 10^{23} nuclei and even more electrons. Symmetry can be used to reduce the degrees of freedom drastically, but still an alternative way of calculating the system's observables is needed. While methods like Hartree-Fock theory aim at an approximation of the wave function, density functional theory (DFT) uses a very different approach, where the electronic ground state density is used to calculate observables rather than the wave function.

In general, one is not interested in the wave function *per se*, but instead in the expectation values of observables (e.g. the ground state energy). As we will see in Section 2.2, knowledge of the density is sufficient to obtain these expectation values. In fact, this has a profound effect on the computational complexity of the problem. On the one hand the wave function $\psi(\mathbf{r}_1, ..., \mathbf{r}_N)$ depends on 3N variables, since each electron has three coordinates. On the other hand the ground state density $n(\mathbf{r})$ has only three variables, regardless of the number of electrons! This makes large systems much more tractable than in a formalism based on the wave function.

In the next section, we will start by deriving the Hohenberg-Kohn theorem, which forms the basis of DFT. Next, we will present the Kohn-Sham equations, that are commonly used to implement DFT. Finally, the local-density approximation will be discussed in some detail. For more in-depth information there are a number of sources available, in particular Refs. [16, 17, 18, 19]. Below, we will closely follow these references.

2.2 The Hohenberg-Kohn Theorem

The idea of using the electronic ground state density instead of the wave function was first developed independently by both Thomas [20] and Fermi [21] in 1927. However, the formal justification was only given in 1964 by Hohenberg and Kohn [22]. For the proof of the Hohenberg-Kohn theorem we will limit ourselves to a system with a non-degenerate ground state in the absence of external magnetic fields. These restrictions however, can be removed (see e.g. Ref. [18]). The theorem states that the ground state density uniquely

determines the external potential and thus all properties of the system. The proof relies on *reductio ad absurdum.*

Let us consider two systems, labeled 1 and 2, with static single-particle external potentials $v_1(\mathbf{r})$ and $v_2(\mathbf{r})$ that differ by more than a constant, but give the same ground state density $n(\mathbf{r})$. Associated with each system is a Hamiltonian $H_{1,2}$, a ground state wave function $|\psi_{1,2}\rangle$ and a ground state energy $E_{1,2}$, which are all different.
The density is built of electrons at positions $\mathbf{r}_i$

$$\hat{n}(\mathbf{r}) \quad = \quad \sum_i \delta(\mathbf{r} - \mathbf{r}_i) \tag{2.3}$$

and therefore the many-body external potential can be written as

$$\hat{V} \quad = \quad \sum_i v(\mathbf{r}_i) = \int d^3r \; \hat{n}(\mathbf{r}) v(\mathbf{r}). \tag{2.4}$$

If we apply this to our two systems and keep in mind that, according to our assumptions above, ψ_1 and ψ_2 yield the same density, we can write the ground state energy as

$$E_{1,2} = \langle \psi_{1,2} | \hat{H}_{1,2} | \psi_{1,2} \rangle = \langle \psi_{1,2} | \hat{T} + \hat{U} | \psi_{1,2} \rangle + \int d^3r \; n(\mathbf{r}) v_{1,2}(\mathbf{r}). \tag{2.5}$$

At this point the Rayleigh-Ritz minimum principle is used, which says that the expecation value $\langle \psi | \hat{H} | \psi \rangle$ is minimal if $|\psi\rangle$ is the ground state wave function associated with $\hat{H}$. Using the Rayleigh-Ritz minimum principle we obtain

$$\begin{aligned} E_1 \quad &< \quad \langle \psi_2 | \hat{H}_1 | \psi_2 \rangle \\ &= \quad \langle \psi_2 | \hat{T} + \hat{U} | \psi_2 \rangle + \int d^3r \; n(\mathbf{r}) v_1(\mathbf{r}) \\ &= \quad E_2 + \int d^3r \; n(\mathbf{r}) \left(v_1(\mathbf{r}) - v_2(\mathbf{r}) \right). \end{aligned} \tag{2.6}$$

The same reasoning can be applied to arrive at the equation

$$E_2 < E_1 + \int d^3r \; n(\mathbf{r}) \left(v_2(\mathbf{r}) - v_1(\mathbf{r}) \right). \tag{2.7}$$

By adding up equations (2.6) and (2.7), one ends up with a contradiction:

$$E_1 + E_2 < E_1 + E_2. \tag{2.8}$$

One therefore concludes that $|\psi_1\rangle$ and $|\psi_2\rangle$ can not lead to the same ground state density. As a result there exists a one-to-one correspondence between the external potential and the ground state density. The potential determines the Hamiltonian and thus the ground state. Consequently, v and the ground state quantities n and $|\psi\rangle$ determine each other uniquely. In mathematical terms this means that $|\psi\rangle$ is a unique functional of the ground

state density, which will be denoted as $|\psi[n]\rangle$. This functional is *universal* in the sense that $|\psi\rangle$ can in principle be constructed from n, without explicit knowledge of v. It therefore applies to all many-particle systems with the same interaction ($\hat{U}$ was fixed throughout this discussion). Given that the functional $|\psi[n]\rangle$ applies to atoms, molecules and solids, the dependence on n must be highly complicated. In fact the dependence is only known for a few special cases, most notably the free electron gas. It follows directly from the existence of $|\psi[n]\rangle$ that every ground state observable O is itself a functional of the density,

$$O[n] = \langle\psi[n]|\hat{O}|\psi[n]\rangle. \tag{2.9}$$

For the most important observable, the ground state energy, one gets:

$$E[n] = \langle\psi[n]|\hat{H}|\psi[n]\rangle = F[n] + \int d^3r\ v(\mathbf{r})n(\mathbf{r}) \tag{2.10}$$

$$F[n] = \langle\psi[n]|\hat{T}+\hat{U}|\psi[n]\rangle, \tag{2.11}$$

where $F[n]$ is a universal functional of the density for all systems with the same underlying interaction $\hat{U}$.

There is a minimum principle for the ground state energy, which follows from the Rayleigh-Ritz variational principle and the unique mapping between n and $|\psi\rangle$. Let n be the density of the ground state associated with $\hat{H}$ then for any $n' \neq n$ we obtain

$$E[n] = \langle\psi[n]|\hat{H}|\psi[n]\rangle < E[n'] = \langle\psi[n']|\hat{H}|\psi[n']\rangle. \tag{2.12}$$

An elegant formula that automatically includes degenerate states was given by Levy [23]. The ground state energy can be written as

$$\begin{aligned} E &= \min_{|\psi|^2=n} \langle\psi|\hat{T}+\hat{U}+\hat{V}|\psi\rangle \\ &= \min_n \left(F[n] + \int d^3r\ v(\mathbf{r})n(\mathbf{r}) \right), \end{aligned} \tag{2.13}$$

where the search is first over all antisymmetric wave functions yielding $n(\mathbf{r})$ and thereafter over all normalized positive densities. Any wave function that yields the correct density, while also minimizing $\hat{T}+\hat{U}$ corresponds to a ground state. Unfortunately, the exact form of $F[n]$ is not known and thus a minimization with respect to the density as in Eq. (2.13) is not practical. It was only with the advent of the Kohn-Sham equations in 1965 [24] that the ground state density could be computed efficiently. This will be introduced in the next section.

2.3 Kohn-Sham Equations

The basic idea underlying the Kohn-Sham equations is to map a system of interacting electrons onto a fictitious system (the Kohn-Sham system) of non-interacting electrons that generates the same density [1]. Thus the original Hamiltonian in Eq. (2.2) is replaced by a Hamiltonian of independent electrons that contains all many-body effects in the effective Kohn-Sham potential $\hat{V}_{KS}$

$$\hat{H}_{KS} = \hat{T} + \hat{V}_{KS}. \tag{2.14}$$

This results in a set of single-particle equations, the *Kohn-Sham equations*, which are much more tractable than the original fully interacting system.
To derive the Kohn-Sham equations we apply the variational principle to the total energy functional

$$E[n] = F[n] + \int d^3r \; n(\mathbf{r})v(\mathbf{r}) \tag{2.15}$$

and include the Lagrange multiplier ϵ to satisfy the additional constraint that the number of electrons should remain constant

$$\begin{aligned}
\delta E[n] &\stackrel{!}{=} 0 \\
&= \int d^3r \; \frac{\delta}{\delta n(\mathbf{r})} \left[E(n(\mathbf{r})) - \epsilon \left(\int d^3r' \; n(\mathbf{r}') - N \right) \right] \delta n(\mathbf{r}) \\
&= \int d^3r \; \left[\frac{\delta E[n(\mathbf{r})]}{\delta n(\mathbf{r})} - \epsilon \right] \delta n(\mathbf{r}) \\
&= \int d^3r \; \left[\frac{\delta F[n(\mathbf{r})]}{\delta n(\mathbf{r})} + v(\mathbf{r}) - \epsilon \right] \delta n(\mathbf{r}).
\end{aligned} \tag{2.16}$$

The unknown functional $F[n]$ is dealt with by rewriting it in terms of T_0, the kinetic energy of a system of non-interacting electrons, the Coulomb energy and a correction term E_{xc}, that captures exchange and correlation effects

$$F[n] = T_0[n] + \frac{1}{2} \int d^3r \int d^3r' \frac{n(\mathbf{r})n(\mathbf{r}')}{|\mathbf{r} - \mathbf{r}'|} + E_{xc}[n]. \tag{2.17}$$

It follows from equations (2.15) and (2.17) that

$$E_{xc}[n] = T[n] + U[n] - T_0[n] - \frac{1}{2} \int d^3r \int d^3r' \frac{n(\mathbf{r})n(\mathbf{r}')}{|\mathbf{r} - \mathbf{r}'|}. \tag{2.18}$$

[1] At first this seems to conflict with the Hohenberg-Kohn theorem. However, in the proof of the Hohenberg-Kohn theorem (see Eq. 2.6) we implicitly assumed that both systems have the same underlying interaction $\hat{U}$. This is not the case when comparing the non-interacting Kohn-Sham system with the real physical system.

Introducing the Hartree potential v_H, the exchange-correlation potential v_{xc} and the Kohn-Sham potential v_{KS}

$$v_H(\mathbf{r}) = \int d^3r' \frac{n(\mathbf{r}')}{|\mathbf{r}-\mathbf{r}'|} \tag{2.19}$$

$$v_{xc}(\mathbf{r}) = \left.\frac{\delta E_{xc}[n(\mathbf{r})]}{\delta n(\mathbf{r})}\right|_{n=n_0} \tag{2.20}$$

$$v_{KS}(\mathbf{r}) = v_H(\mathbf{r}) + v(\mathbf{r}) + v_{xc}(\mathbf{r}) \tag{2.21}$$

Eq. (2.16) can be rewritten to yield

$$\delta E[n(\mathbf{r})] = \int d^3r \left[\left.\frac{\delta T_0[n(\mathbf{r})]}{\delta n(\mathbf{r})} + v_{KS}(\mathbf{r})\right|_{n=n_0} - \epsilon\right] \delta n(\mathbf{r}) = 0. \tag{2.22}$$

Since this equation looks like an equation for non-interacting particles, there must be single-particle functions $\{\phi_j\}$ solving it. The corresponding single-particle Schrödinger equation is called Kohn-Sham equation:

$$\left[-\frac{\Delta}{2} + v_{KS}(\mathbf{r})\right] \phi_j(\mathbf{r}) = \epsilon_j \phi_j(\mathbf{r}). \tag{2.23}$$

The Kohn-Sham orbitals $\{\phi_j\}$ are the solutions of the fictitious Kohn-Sham system and must not be mistaken for solutions of the physical system, although of course they yield the same density

$$n(\mathbf{r}) = \sum_{j=1}^{N} |\phi_j(\mathbf{r})|^2. \tag{2.24}$$

Both of these equations, (2.23) and (2.24), have to be solved in a self-consistent manner. Starting with an initial guess for $v_{KS}(\mathbf{r})$, the Kohn-Sham equations are solved and the density is calculated using the Kohn-Sham wave functions. The resulting density is used to arrive at a new guess for the Kohn-Sham potential according to Eqs. (2.19), (2.20) and (2.21), which is then used to repeat the cycle until both the Kohn-Sham potential and the density are converged.

We arrive at an expression for the ground state energy by multiplying Eq. (2.23) with $\phi_j^*(\mathbf{r})$ from the left, integrating over all three dimensions of space and summing over all electrons j

$$E[n] = -\sum_{j=1}^{N} \int d^3r\ \phi_j^*(\mathbf{r}) \frac{\Delta}{2} \phi_j(\mathbf{r}) + \int d^3r\ v_{KS}(\mathbf{r}) n(\mathbf{r}) \tag{2.25}$$

$$= -\sum_{j=1}^{N} \int d^3r\ \phi_j^*(\mathbf{r}) \frac{\Delta}{2} \phi_j(\mathbf{r}) + \frac{1}{2} \int d^3r\ d^3r' \frac{n(\mathbf{r}) n(\mathbf{r}')}{|\mathbf{r}-\mathbf{r}'|} + \int d^3r\ v(\mathbf{r}) n(\mathbf{r}) + E_{xc}[n].$$

So far no approximations have been made to arrive at the Kohn-Sham equations, because the Kohn-Sham potential $v_{KS}(\mathbf{r})$ contains all many-body effects. Therefore the Kohn-Sham equations are exact, though in practice an explicit expression for $E_{xc}[n]$ is generally not available. Although its contribution to the total energy is much smaller than $T_0[n]$ or $U[n]$ it is of critical importance to get a good approximation for $E_{xc}[n]$. To illustrate this point it is enough to look at Thomas-Fermi theory. It takes the kinetic energy of a free electron gas, but it misses both exchange and correlation effects. The consequences are dramatic. There is no atomic shell structure and no binding for molecules or solids in Thomas-Fermi theory [25].

Over the years several types of approximations to $E_{xc}[n]$ have been developed, with ever-increasing computational complexity. These are commonly referred to as the five rungs on "Jacob's Ladder" and correspond to different choices of ingredients that are taken into account:

1. The *local-density approximation* (LDA) constitutes the simplest approximation, because it uses only the density $n(\mathbf{r})$.
2. The *generalized gradient approximation* (GGA) uses both the density $n(\mathbf{r})$, as well as its gradient $\nabla n(\mathbf{r})$. The PBE functional developed by Perdew, Burke and Ernzerhof [26] is perhaps the most famous example of this category.
3. The *meta-GGAs* further add $\Delta n(\mathbf{r})$, as well as the Kohn-Sham orbital kinetic-energy density τ. An example would be the TPSS functional [27].
4. The *hyper-GGAs* add the exact exchange energy density, which is a nonlocal functional of the Kohn-Sham orbitals. Since the Kohn-Sham orbitals are themeselves fully determined by the density, hyper-GGAs still count as true DFT functionals. Hybrid functionals like PBE0 [28] can be considered part of this group. They are based on GGAs, but also incorporate a fraction of exact exchange.
5. The last rung on the ladder includes also the unoccupied Kohn-Sham orbitals. An example of this would be the random phase approximation (RPA) [29].

Here, we will focus only on LDA, the approximation that was used in this work. LDA has several remarkable properties, while being deceptively simple, which we will review in some detail in the next section.

2.4 Local-density Approximation

The local-density approximation was developed by Kohn and Sham [24]. It represents the simplest approximation for taking exchange and correlation effects into account. Despite it's simplicity it is remarkably accurate for atomic and molecular ground state energies (error less than 0.5%), molecular equilibrium distances (error less than 5%) and lattice constants (systematic overbinding by less than 3%)[30]. The success of LDA can be

explained, to some extent, in terms of a cancellation of errors. This will be discussed towards the end of this section in terms of the spherically averaged exchange-correlation hole (XC hole), but first we introduce LDA.

Consider a slowly varying density. This system can be regarded as a collection of small volumes d^3r each containing a homogenous electron gas, with neighbouring volumes having similar densities. Then $E_{xc}[n]$ is given by

$$E_{xc}^{LDA}[n] = \int d^3r \; n(\mathbf{r})\epsilon_{xc}(n(\mathbf{r})), \tag{2.26}$$

with $\epsilon_{xc}(n(\mathbf{r}))$ being the exchange-correlation energy per particle for a homogenous electron gas. $\epsilon_{xc}(n(\mathbf{r}))$ is multiplied by the number of particles in each infinitesimal volume element $n(\mathbf{r})d^3r$ and summed over the total volume. An important subtlety is the fact that $\epsilon_{xc}(n(\mathbf{r}))$ is not a functional of the density, but rather a function of the density at a particular point $\mathbf{r}$.

In solid-state physics and DFT in particular, the homogenous electron gas is an important model and LDA solves it exactly. We separate $\epsilon_{xc}(n(\mathbf{r}))$ into an exchange part ϵ_x and a correlation part ϵ_c:

$$\epsilon_{xc}(n(\mathbf{r})) \quad = \quad \epsilon_x(n(\mathbf{r})) + \epsilon_c(n(\mathbf{r})) \tag{2.27}$$

For this system the exchange energy per electron $\epsilon_x(n(\mathbf{r}))$ is known exactly [16]:

$$\epsilon_x(n(\mathbf{r})) \quad = \quad \frac{3k_F}{4\pi}, \tag{2.28}$$

where $k_F = (3\pi^2 n)^{1/3}$ is the Fermi wave vector.
Analytic expressions for the correlation part are known only in the high- and low-density limits. A frequently used measure for the density is the Wigner-Seitz radius

$$r_s = \left[\frac{3}{4\pi n(\mathbf{r})}\right]^{\frac{1}{3}}, \tag{2.29}$$

which is the radius of a sphere around each electron such that the combined volume of all spheres equals the total electron density. Thus, $r_s \to 0$ corresponds to the *high*-density limit and $r_s \to \infty$ is the *low*-density limit. Using this measure for the density the exact analytic expressions are written as follows [19]:

In the high-density limit ($r_s \to 0$) we have

$$\epsilon_c(r_s) = 0.0311 \; \ln(r_s) - 0.047 + 0.009 r_s \ln(r_s) - 0.017 r_s + ... \tag{2.30}$$

and the low-density limit ($r_s \to \infty$) reads

$$\epsilon_c(r_s) = -\frac{0.896}{r_s} + \frac{1.325}{r_s^{\frac{3}{2}}} + ... \tag{2.31}$$

Early on Wigner [31] suggested an interpolation formula

$$\epsilon_c(r_s) = -\frac{0.44}{7.8 + r_s} \tag{2.32}$$

that works well in the range of $1 \leq r_s \leq 6$, despite the fact that it ignores, among other things, the leading logarithmic high-density term. Nowadays known exact limiting values are combined with accurate Quantum Monte-Carlo calculations (e.g. Ceperley and Alder [32]), to obtain the correlation term for arbitrary densities.

An alternative way of thinking about correlation is by means of an enhancement factor over the exchange part

$$\epsilon_{xc}(r_s) = F_{xc}(r_s)\epsilon_x(r_s). \tag{2.33}$$

In the high-density limit, where r_s is small, exchange is much larger than correlation and thus $F_{xc}(r_s \to 0) = 1$. In the limit of large r_s however, correlation becomes comparable to exchange leading to $F_{xc}(r_s \to \infty) = 1.896$ [16].

Historically, the local-density approximation was introduced using a slowly varying density. Thus it came as a surprise when LDA turned out to work remarkably well for systems with rapidly varying densities, such as atoms and molecules. This unexpected finding can be attributed in part to the fact that LDA satisfies some important constraints that hold for the exact exchange-correlation functional. First, LDA is *size consistent*, meaning that

$$E_{xc}[n_A + n_B] = E_{xc}[n_A] + E_{xc}[n_B], \tag{2.34}$$

if the densities n_A and n_B do not overlap. Second, upon coordinate scaling by a factor γ, the normalization of the density and thus the number of electrons is preserved under LDA:

$$n_\gamma(\mathbf{r}) = \gamma^3 n(\gamma\mathbf{r}). \tag{2.35}$$

If the density is squeezed ($\gamma < 1$) or stretched ($\gamma > 1$), the exchange part scales correctly, according to

$$E_x[n_\gamma] = \gamma E_x[n], \tag{2.36}$$

whereas the correlation part in LDA scales accurately only in the low-density limit. Third, LDA obeys an important constraint first proved by Lieb and Oxford [33]

$$E_{xc}[n] \geq 2.273\ E_x^{LDA}[n]. \tag{2.37}$$

Lastly, the success of LDA can be understood in terms of what is called the exchange-correlation hole (XC hole). The complete derivation would go beyond the scope of this thesis. Here, we will restrict ourselves to a short outline and refer the reader to Ref. [18] for the details.

The concept of an XC hole arises out of the two-particle reduced density matrix $\rho(\mathbf{r}, \mathbf{r}')$ and yields the expression

$$\rho(\mathbf{r}, \mathbf{r}') = n(\mathbf{r}) n_2(\mathbf{r}, \mathbf{r}'), \tag{2.38}$$

where $n_2(\mathbf{r}, \mathbf{r}')$ is the density of electrons at $\mathbf{r}'$, given that there is an electron at $\mathbf{r}$. Clearly then

$$\int d^3r'\ n_2(\mathbf{r}, \mathbf{r}') = N - 1. \tag{2.39}$$

The XC hole $n_{xc}^{\lambda}(\mathbf{r}, \mathbf{r}')$ is defined by writing $n_2(\mathbf{r}, \mathbf{r}')$ as

$$n_2(\mathbf{r}, \mathbf{r}') = n(\mathbf{r}') + n_{xc}^{\lambda}(\mathbf{r}, \mathbf{r}'), \tag{2.40}$$

where λ is the coupling constant. In this formalism $\lambda = 0$ corresponds to the Kohn-Sham system with its independent particles, whereas $\lambda = 1$ corresponds to the physical system. Systems with $0 < \lambda < 1$ serve as convenient mathematical fictions. For a given λ the wave function $|\psi_\lambda\rangle$ is defined as the antisymmetric wave function that yields density $n(\mathbf{r})$ and minimizes the expectation value of $\hat{H}_\lambda = \hat{T} + \lambda\hat{U} + \hat{V}$.

As can be seen from the definition and the sum rule for $n_2(\mathbf{r}, \mathbf{r}')$ one gets

$$\int d^3r'\ n_{xc}^{\lambda}(\mathbf{r}, \mathbf{r}') = -1, \tag{2.41}$$

which justifies the interpretation of $n_{xc}^{\lambda}(\mathbf{r}, \mathbf{r}')$ as a hole. Averaging over the coupling constant gives

$$\overline{n}_{xc}(\mathbf{r}, \mathbf{r}') = \int_0^1 d\lambda n_{xc}^{\lambda}(\mathbf{r}, \mathbf{r}'). \tag{2.42}$$

It can be shown [18] that a general exact equation for $E_{xc}[n]$ is

$$E_{xc}[n] \quad = \quad \frac{1}{2} \int d^3r d^3r'\ \frac{n(\mathbf{r})\overline{n}_{xc}(\mathbf{r},\ \mathbf{r}')}{|\mathbf{r} - \mathbf{r}'|}, \tag{2.43}$$

which can be interpreted as a simple electrostatic interaction between the density and the coupling-constant averaged XC hole $\overline{n}_{xc}(\mathbf{r},\ \mathbf{r}')$. For further analysis we define $s = |\mathbf{r} - \mathbf{r}'|$ and do a multipole expansion of $\overline{n}_{xc}(\mathbf{r}, \mathbf{r}')$:

$$\overline{n}_{xc}(\mathbf{r}, \mathbf{r}') = \overline{n}_{xc}(\mathbf{r}, s) = \sum_{lm} \overline{n}^{xc}_{lm}(\mathbf{r}, s) Y_{lm}(\Omega). \tag{2.44}$$

The reason for this expansion is the insight that $E_{xc}[n]$ depends only on the spherical-symmetric part of the XC hole $\overline{n}^{xc,LDA}_{00}(\mathbf{r}, s)$ [18]. This turns out to be very important for the success of LDA, because even though

$$\overline{n}_{xc}(\mathbf{r}, \mathbf{r}') \neq \overline{n}^{LDA}_{xc}(\mathbf{r}, \mathbf{r}') \tag{2.45}$$

the spherically symmetric parts are approximately equal [30]

$$\overline{n}^{xc}_{00}(\mathbf{r}, s) \approx \overline{n}^{xc,LDA}_{00}(\mathbf{r}, s), \tag{2.46}$$

which helps to explain the accuracy of LDA.

3 Numerical Methods

So far we have introduced the Kohn-Sham equations. Now we will describe how they are put into practice.

The choice of the basis set has a critical impact on both the accuracy as well as the computational cost. When dealing with crystal structures, which are subject to periodic boundary conditions, it is convenient to use planewaves as a basis set. They form an orthogonal and complete basis set, which can be treated in reciprocal space with relatively little computational effort. However, close to the nucleus, where the potential varies strongly, a large number of planewaves is required. A common way of dealing with this is through the use of pseudopotentials, which keeps the number of planewaves lower, but this comes at the cost of less accurate results.

In this work, we use the `exciting` code [34], which is particularly accurate because of two related features. First, all electrons are taken into account explicitly. Second, no shape approximation to the potential is made. The most appropriate basis functions are augmented planewaves (APW).

The APW methods are among the most precise schemes for numerically solving the Kohn-Sham equations. Actually, several methods are grouped together under the general term "APW", which will be introduced below. In this approach atomic-like wave functions are used in the vicinity of the nuclei, while planewaves are used in the region where the potential varies more slowly. Such a basis enables higher accuracy compared to the pseudopotential approach at the cost of a higher computational effort.

Starting from the actual APW basis we go on to a modification that "expands" the basis around a given energy, called LAPW. Subsequently, we also include local orbitals into the basis.

Generally, the Kohn-Sham orbitals ϕ_i can be expanded using a basis φ_j and expansion coefficients C_{ij} in the following manner:

$$\phi_i(\mathbf{r}) = \sum_j C_{ij}\varphi_j(\mathbf{r}). \tag{3.1}$$

We insert this expansion into the Kohn-Sham Eqs. (2.23), multiply by φ_k^* from the left, and integrate over $\mathbf{r}$ to arrive at the generalized eigenvalue problem

$$\sum_j H_{kj} C_{ji} = \epsilon_i \sum_j S_{kj} C_{ji}. \tag{3.2}$$

H_{kj} denotes the matrix elements of the single-particle hamiltonian $\hat{h}(\mathbf{r})$:

$$H_{kj} = \int d^3r \; \varphi_k^*(\mathbf{r}) \; \hat{h}(\mathbf{r}) \; \varphi_j(\mathbf{r}), \tag{3.3}$$

with

$$\hat{h}(\mathbf{r}) = -\frac{\Delta}{2} + v_{KS}(\mathbf{r}). \tag{3.4}$$

For a non-orthonormal basis set, we also have the overlap matrix elements, which read:

$$S_{kj} = \int d^3r \; \varphi_k^*(\mathbf{r}) \varphi_j(\mathbf{r}). \tag{3.5}$$

3.1 The Augmented-planewave Basis

The idea underlying the APW method is a separation of space into two types of regions (see Fig. (3.1)). Centered around the nuclei are so-called *muffin-tin spheres* (MT), where the basis set consists of atomic-like functions. In general, the size of the MT will not be the same for all atoms, but will depend on the size of the nucleus. In between the muffin-tins lies the *interstitial region* (I), where planewaves with volume Ω are used. The stronger the charge distribution varies outside of the muffin-tins, the more planewaves are required.

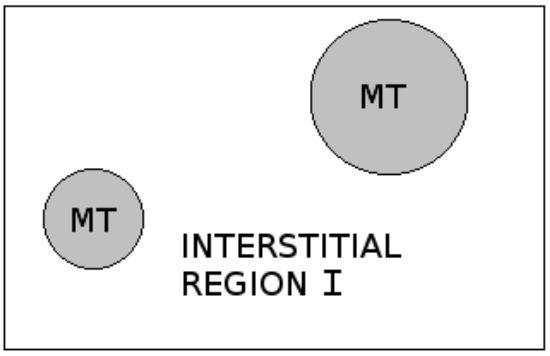

Figure 3.1: Partitioning of the unit cell into MTs and the interstitial region.

The APW basis has the form:

$$\varphi_{\mathbf{G}+\mathbf{k}}(\mathbf{r}) = \begin{cases} \sum_{lm} A_{lm\alpha}^{\mathbf{G}+\mathbf{k}} u_{l\alpha}(r_\alpha) Y_{lm}(\hat{\mathbf{r}}_\alpha) & \text{if } r_\alpha \leq R_{MT}^\alpha \\ \frac{1}{\sqrt{\Omega}} e^{i(\mathbf{G}+\mathbf{k})\mathbf{r}} & \text{if } \mathbf{r} \in I. \end{cases} \tag{3.6}$$

For atom α positioned at $\mathbf{R}_\alpha$ the wave function $\varphi_{\mathbf{G}+\mathbf{k}}(\mathbf{r})$ inside the muffin-tin radius R_{MT}^α is expanded in terms of spherical harmonics $Y_{lm}(\hat{\mathbf{r}}_\alpha)$ and radial functions $u_{l\alpha}(r_\alpha)$, with the coefficients $A_{lm\alpha}^{\mathbf{G}+\mathbf{k}}$. $\mathbf{G}$ is the reciprocal lattice vector, $\mathbf{k}$ is the wave vector in the first Brillouin zone and $\mathbf{r}_\alpha = \mathbf{r} - \mathbf{R}_\alpha$. The radial functions $u_{l\alpha}(r_\alpha)$ are obtained by

solving the radial Schrödinger equation:

$$\left[-\frac{1}{2}\frac{\partial^2}{\partial r_\alpha^2}+\frac{l(l+1)}{2r_\alpha^2}+v_{KS}(r_\alpha)-\epsilon_l\right](r_\alpha u_{l\alpha}(r_\alpha))=0, \tag{3.7}$$

with the spherically averaged Kohn-Sham potential $v_{KS}(r_\alpha)$. The coefficients $A_{lm\alpha}^{\mathbf{G}+\mathbf{k}}$ are determined by the condition that the functions used for the muffin-tin must match the value of the planewaves on the surface of the muffin-tin, to ensure that the basis set is continuous at the boundary.

The Kohn-Sham potential is expanded in a similar fashion:

$$v_{KS}(\mathbf{r})=\begin{cases}\sum_{lm}V_{lm}(r)Y_{lm}(\hat{\mathbf{r}}) & \mathbf{r}\in \text{MT}\\ \sum_{\mathbf{G}}V_{\mathbf{G}}e^{i\mathbf{G}\mathbf{r}} & \mathbf{r}\in \text{I}.\end{cases} \tag{3.8}$$

Although, in principle, the APW approach seems like an ideal solution, in practice there is a problem. As can be seen from the radial Schrödinger Eq. (3.7), the radial functions depend on ϵ_l. Thus, we are dealing with a nonlinear eigenvalue problem. Starting with a guess for ϵ_l, the APW basis is constructed and Eq. (3.2) is diagonalized. This procedure would have to be repeated until the eigenvalues are converged. Clearly a more efficient process is desired. One way of linearizing the eigenvalue probem was developed by Andersen [35] resulting in the linearized augmented planewave (LAPW) method.

3.2 The Linearized Augmented-planewave Method

In LAPW each radial function $u_l(r_\alpha,\epsilon)$ can be viewed as an expansion around ϵ_l, which does not have to be a Kohn-Sham energy:

$$\begin{aligned} u_l(r_\alpha,\epsilon) &\approx u_l(r_\alpha,\epsilon_l)+\dot{u}_l(r_\alpha,\epsilon_l)(\epsilon-\epsilon_l), \\ \text{where } \dot{u}_l(r_\alpha,\epsilon_l) &= \left.\frac{\partial u_l(r_\alpha,\epsilon)}{\partial\epsilon}\right|_{\epsilon=\epsilon_l}. \end{aligned} \tag{3.9}$$

The error in the radial functions is of the order $\mathcal{O}[(\epsilon-\epsilon_l)^2]$, and the error in the total energy is of the order $\mathcal{O}[(\epsilon-\epsilon_l)^4]$. As a result, one can get accurate energies with a fairly broad range of linearization energies ϵ_l. Typically, ϵ_l is choosen to lie in the middle of the corresponding l-like band in order to minimize the error resulting from the linearization. The energy derivatives $\dot{u}_l(r_\alpha,\epsilon_l)$ are taken into account:

$$\varphi_{\mathbf{G}+\mathbf{k}}(\mathbf{r})=\begin{cases}\sum_{lm}[A_{lm}^{\alpha}(\mathbf{G}+\mathbf{k})u_l(r_\alpha,\epsilon_l)+B_{lm}^{\alpha}(\mathbf{G}+\mathbf{k})\dot{u}_l(r_\alpha,\epsilon_l)]Y_{lm}(\hat{\mathbf{r}}_\alpha) & r_\alpha\le R_{MT}^{\alpha}\\ \frac{1}{\sqrt{\Omega}}e^{i(\mathbf{G}+\mathbf{k})\mathbf{r}} & \mathbf{r}\in I.\end{cases}$$

The coefficients $A_{lm}^{\alpha}(\mathbf{G}+\mathbf{k})$ and $B_{lm}^{\alpha}(\mathbf{G}+\mathbf{k})$ are choosen in a way that ensures the continuity of the basis function at the surface of the muffin-tin, i.e. to match the planewaves used in the interstitial region. To determine the $\dot{u}_l(r_\alpha,\epsilon_l)$ one must solve the equation

resulting from the energy derivative of the radial Schrödinger Eq. (3.7)

$$\left[-\frac{1}{2}\frac{\partial^2}{\partial r_\alpha^2}+\frac{l(l+1)}{2r_\alpha^2}+v_{KS}(r_\alpha)\right]\dot{u}_l(r_\alpha,\epsilon_l)=r_\alpha[u_l(r_\alpha,\epsilon_l)+\epsilon_l\dot{u}_l(r_\alpha,\epsilon_l)]. \tag{3.10}$$

In the spirit of a Taylor expansion the nonlinear problem is transformed into a linear one, which makes the calculations more tractable, because only one diagonalization is needed for a given Kohn-Sham potential. However, the single diagonalization comes at the price of a more complicated basis set. The continuity in the first derivative requires a higher planewave cutoff G_{max} compared to APW, i.e. a larger basis set. We will come back to this when discussing convergence tests in Chapter 4. An additional approach using local orbitals has been proposed by Sjöstedt *et al.* [36], which can overcome these problems and is used throughout this work.

3.3 The APW+lo Basis

One can combine APW with local orbitals (lo), resulting in the APW+lo basis set. The local orbitals are defined as:

$$\varphi_{lm}^{\alpha,lo}(\mathbf{r})=\begin{cases}[a_{lm}^\alpha u_l(r_\alpha,\epsilon_l)+b_{lm}^\alpha\dot{u}_l(r_\alpha,\epsilon_l)]Y_{lm}(\hat{\mathbf{r}}_\alpha) & r_\alpha\le R_{MT}^\alpha\\ 0 & \mathbf{r}\in I.\end{cases} \tag{3.11}$$

The radial functions $u_l(r_\alpha,\epsilon_l)$ use the same fixed energy ϵ_l, as the corresponding APW orbital. The coefficients a_{lm}^α and b_{lm}^α are determined by the normalization of the wave function and the requirement that it must vanish at the surface of the muffin-tin in both its value and spatial derivative. The local orbitals are only used for particularly relevant states, like those whose angular momentum l is such that the energies are close to the Fermi level. Along with the fact that the local orbitals do not have to obey any matching conditions with planewaves, this results in only a slightly increased basis set and therefore the matrix sizes in Eq. (3.2) are kept under control.

4 Preparatory Steps

We discuss the numerical accuracy with respect to the basis set size and the **k**-point mesh. Following this, the structure-optimization algorithms are described. Finally, we assess whether it is valid to approximate the LT phase by a unit cell that contains two molecules instead of four.

4.1 Convergence on the Basis Set Size

As expressed in Chapter 3, the accuracy of a calculation depends on the type and size of the basis set that is employed. The planewave cutoff G_{max} determines the size of the basis in the interstitial region. However, within APW methods this parameter is meaningful only when considered in combination with the size of the muffin-tin radii, which define the region close to the nuclei. The smallest muffin-tin radius R_{MT}^{min}, combined with the planewave cutoff G_{max}, defines a dimensionless cutoff parameter, which in `exciting` is called

$$\texttt{rgkmax} = R_{MT}^{min}\, G_{max}. \tag{4.1}$$

While `rgkmax` is one of the most important parameters for accurate calculations, high values of `rgkmax` are costly. In fact, the computational time scales approximately like $t \sim \texttt{rgkmax}^9$ [37]. In systems with multiple atomic species it is important to make a distinction between the input parameter $\texttt{rgkmax} = R_{MT}^{min} G_{max}$, where the *smallest* muffin-tin radius is used, and $R_{MT}^{\alpha} G_{max}$, which is a local basis set cutoff that depends on the species of atom α. For a given `rgkmax` the smallest muffin-tin radius determines the size of the planewave basis set. Atomic species with larger muffin-tin radius use the same number of planewaves but have a higher basis set cutoff, due to the increased muffin-tin radius.

In this work the smallest muffin-tin pertains to hydrogen with $R_{MT}^{H} = R_{MT}^{min} = 0.75$, whereas the largest muffin-tin radius belongs to sulfur ($R_{MT}^{S} = 1.75$). Thus, a value of $\texttt{rgkmax} = 5$, which is sufficient for hydrogen, corresponds to an effective rgkmax for sulfur of 12, which is very well converged. This work concerns the relative phase stability of the HT and LT polymorphs of 6T, as well as a transition barrier between them. Our main focus is on total energy *differences*, rather than on absolute values. Fig. (4.1) shows the convergence of the energy difference between the two phases with respect to `rgkmax`. The energy corresponding to $\texttt{rgkmax} = 5.5$ is set to zero. At $\texttt{rgkmax} = 5.0$ the energy difference is converged within 0.2 meV. Hence, we use `rgkmax`=5.0 for all the results presented in this thesis.

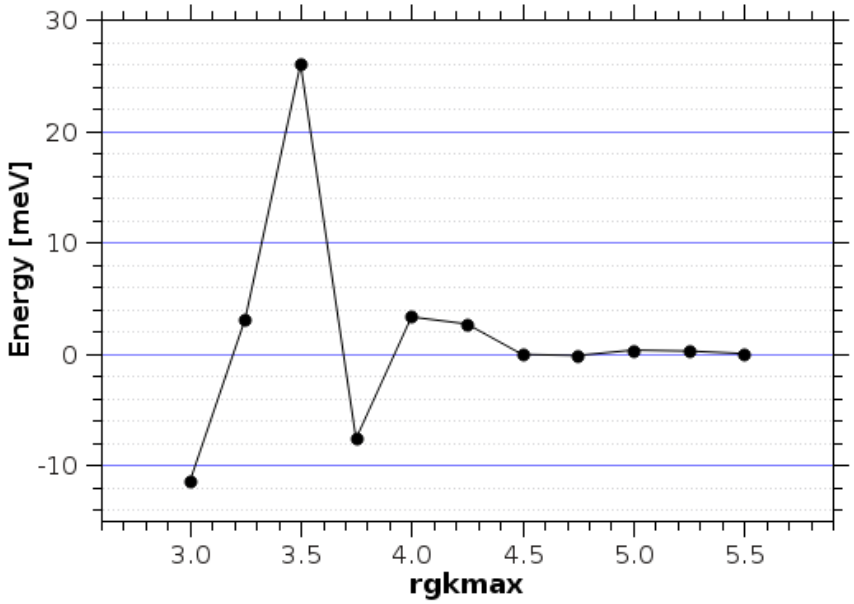

Figure 4.1: Convergence with respect to `rgkmax`. The plot shows the difference in ground state energies between the HT and LT phases of sexithiophene for several values of `rgkmax`. The energies scale is chosen, such that the value at `rgkmax` = 5.5 corresponds to 0 meV.

4.2 Convergence on the k-point Grid

When dealing with crystal structures, there are many operations that involve integrations in reciprocal space. In practice the integrals have to be approximated by a sum over a discrete grid of **k**-points. The choice of the **k**-mesh is important not only as a parameter for converging the relevant quantities, most notably the total energy, but also in terms of the computational cost. To get the most accurate result for a given number of **k**-points one has to take into account the size and shape of the unit cell. The general principle for allocating **k**-points along each of the basis vector directions is based on the reciprocal relationship between real space and **k**-space: The larger the spatial extent in a given direction is, the lower the number of **k**-points n_{k_i} thas has to be sampled along direction $i = x, y, z$.

To minimize the computational effort the crystal symmetries are taken into account. Some of the **k**-points are equivalent because of these symmetries, leading to a smaller set of *irreducible* **k**-points that have to be sampled, without sacrificing any accuracy. In Tab.

(4.1) an example of the **k**-mesh convergence is shown for 6T-HT. The difference in the

$n_{k_x} \times n_{k_y} \times n_{k_z}$	N_K	E_{HT}^{mol} [eV]
$3 \times 5 \times 1$	6	-89895.883$\underline{7}$10
$6 \times 10 \times 2$	48	-89895.883$\underline{2}$71

Table 4.1: **k**-point convergence of sexithiophene in the high-temperature phase (6T-HT). N_K is the number of irreducible **k**-points. The first deviating digit in the total energy per molecule E_{HT}^{mol} is underlined. Calculations are performed at `rgkmax`=4.0.

energies is only 0.4 meV, although the second grid has 8 times as many **k**-points. This error is comparable to the uncertainty of the convergence with respect to `rgkmax`. From this it follows that the smaller $3 \times 5 \times 1$ grid is sufficient for the HT phase to ensure converged results. An equivalent number of **k**-points is used for the LT phase, namely $(1 \times 3 \times 4)$

4.3 Relaxation of the Atomic Coordinates

To get accurate ground state energies we have to start by minimizing the forces acting on the atoms. In `exciting` three methods are available for this purpose. In the following we present an overview. Additional details are provided in Ref. [34] and references therein. The simplest one is called `newton`. For every optimization step m, each atomic position $\mathbf{R}_\alpha^{m+1}$ is displaced according to

$$\mathbf{R}_\alpha^{(m+1)} = \mathbf{R}_\alpha^{(m)} + \tau_\alpha^{(m)} \left(\mathbf{F}_\alpha^{(m)} + \mathbf{F}_\alpha^{(m-1)} \right). \tag{4.2}$$

The step length is proportional to $\tau_\alpha^{(m)}$, which is initially set to a parameter $\tau_\alpha^{(m)} = \tau_{newton}$. After two successive steps, if the forces have the same sign, $\tau_\alpha^{(m)}$ is increased by τ_{newton}, otherwise it is reset to τ_{newton}.

The method called `harmonic` is an extension of `newton` and based on the harmonic approximation. Contrary to `newton`, all cartesian components of the atomic positions are treated independently. For each component i the `newton` method is used, as long as the ratio of subsequent forces μ is such that

$$\mu = \frac{F_{\alpha,i}^{(m)}}{F_{\alpha,i}^{(m-1)}} \in [0, 3], \tag{4.3}$$

otherwise a harmonic step is taken and the atomic positions are updated according to

$$R_{\alpha,i}^{(m+1)} = \frac{R_{\alpha,i}^{(m-1)} - \mu R_{\alpha,i}^{(m)}}{1-\mu}. \tag{4.4}$$

The third method is the limited-memory version of the Broyden-Fletcher-Goldfarb-Shanno algorithm [38], called `bfgs` in `exciting`. Based on an approximated inverse Hessian matrix for the energy as a function of atomic positions, `bfgs` tries to predict the equilibrium configuration. Each cartesian component i of the atomic positions is allowed to vary within a range determined by the parameter τ_{bfgs} such that

$$R_{\alpha,i}^{(m)} \in \left[R_{\alpha,i}^{(0)} - \tau_{bfgs}, R_{\alpha,i}^{(0)} + \tau_{bfgs}\right]. \tag{4.5}$$

This algorithm is the method of choice, especially far from equilibrium, because it minimizes the forces most effectively. Close to the equilibrium, typically only bond lengths need to be adjusted and therefore `harmonic` can be more convenient than `bfgs`, since it avoids oscillations around the equilibrium.

4.4 Approximation for 6T-LT

So far, we have been concerned with general considerations that apply to any system. Here, we turn to an approximation which is specific to the system studied in this work.

We have seen in Section 1.5 that the LT phase of 6T consists of four molecules/unit cell, compared to the HT unit cell, which only has two molecules/unit cell. Since each molecule of sexithiophene ($C_{24}H_{14}S_6$) consists of 44 atoms, these are fairly large systems. Fortunately, it turns out that the two halves of the LT structure are almost identical. This suggests an approximation of cutting the LT unit cell into halves. To test the validity of this approximation the ground state energies are calculated for both halves individually (denoted LTr_1 and LTr_2, see Tab. (4.2)). The total energies per molecule of the two halves differ by $\Delta E = 0.2$ meV. This is comparable to the uncertainty with respect to the **k**-mesh and `rgkmax`. This small energy difference ΔE justifies the approximation.

$E_{LTr_1}^{mol}$ [eV]	$E_{LTr_2}^{mol}$ [eV]
-89896.111498	-89896.111732

Table 4.2: Total energy per molecule of the unrelaxed halves of 6T-LT, labeled as LTr_1 and LTr_2. The first deviating digit in the total energy is underlined. Calculations are perfomed at `rgkmax`=5.0 with a $1\times 3\times 4$ **k**-point grid.

The energy per molecule from each individual half can be viewed as an upper limit for the actual system with 4 molecules per cell. If either half were lower in energy, this would

constitute the stable structure and the actual LT phase would not be observed. The small ΔE suggests that the choice of which half is used for calculations is not important. From now on only the LTr_1 structure will be used, which is labeled simply as LTr.

5 Results I: Relative Phase Stability

In this chapter we focus on the HT and LT polymorphs of sexithiophene. First, we investigate the relative stability of the two phases and provide a lower bound of the energy difference between both polymorphs. Then, we study the electronic properties of both systems.

5.1 Energetics

Starting from the unrelaxed structures we find the LT phase to be more stable than the HT phase (see Tab. 5.1). The difference in total energies per molecule ΔE_{mol} is 200 meV

	E_{HT}^{mol} [eV]	E_{LTr}^{mol} [eV]	ΔE^{mol} [meV]
Unrelaxed structures	-89895.913	-89896.1118	199.2
Relaxed structures	-89896.756	-89896.7924	36.5

Table 5.1: Total energy per molecule of the unrelaxed and relaxed HT and LTr structures. ΔE^{mol} is the difference in energy per molecule between the two phases. The unrelaxed structures are based on Ref. [12] (HT) and Ref. [13] (LT)

and 37 meV for the experimental and relaxed structures, respectively. This result is in agreement with the experimental observation that the LT phase is the more stable one [14]. Pithan *et al.* studied thin films of sexithiophene and found that the phases desorb at around 200 °C (HT) and 240 °C (LT), respectively [14]. The higher thermal stability of the LT phase suggests that this polymorph should be energetically favored over the HT phase. The difference in desorption temperatures corresponds to 3.4 meV, which is an order of magnitude lower than the difference in total energies between the two phases. However, these values are not directly comparable to our results, given that desorption occurs at the surface where molecules are less strongly bound.

For comparison, we can look at quarterthiophene (4T). Here, the 4T-HT phase is energetically favored over the 4T-LT one, even though it is usually the latter phase that is observed [39]. This is explained by the fact that the stability is temperature-dependent (see Section 1.2). The 4T-HT phase becomes more stable only at temperatures above 191 °C, which is close to the melting point of 214 °C. However, the situation is different than in sexithiophene, where the HT phase desorbs at temperatures much lower than the

melting point of 304 °C [40].

To the best of our knowledge, only one paper has adressed the question of relative stability of the two polymorphs theoretically. Based on force field calculations, Della Valle *et al.* found the HT phase to be favored by 15 meV per molecule over the LT phase [15]. This is in conflict with our finding. Obviously, the difference between our *first-principles* approach and the *classical* force field method of Della Valle *et al.* should account for much of the discrepancy. The sensitivity of the results to the computational method has to do with the fact that we are looking at energy differences that are six orders of magnitude smaller than the total energies. Based on the convergence tests of Chapter 4 our error is on the order of 0.1 meV, much smaller than the energy difference between polymorphs (36.5 meV). Since our results are well-converged let us address the possibility of any other source of error.

Our results are based on LDA and therefore do not explicitly account for van der Waals (vdW) forces. Calculations by Nabok *et al.* suggest that LDA underestimates the cohesive energy by roughly 30%, compared to the vdW density functional (vdW-DF) [41]. However, their work indicates that LDA captures the physical picture, since it follows a trend similar to vdW-DF, as seen from the cohesive energy as a function of oligothiophene length (see Fig. 5.1). Moreover, in this work the atomic positions are optimized, while

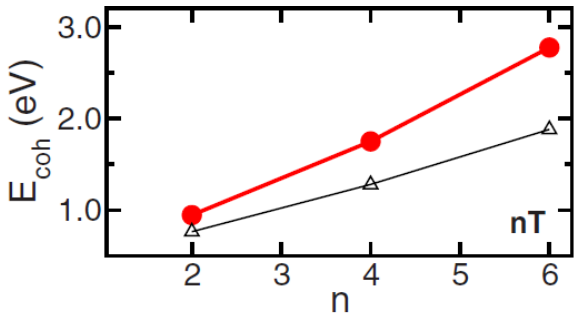

Figure 5.1: Cohesive energies of oligothiophenes (nT) using LDA (triangles) or the vdW density functional (dots). Figure taken from Ref. [41].

the unit cell is kept fixed. For this reason the relaxed structure depends largely on the electrostatic interaction and is well described by LDA. This is also indicated by the study of anthracene by Hummer *et al.* [42]. They found excellent agreement with experiment for the internal geometry over a wide pressure range. Hence, taking vdW forces into account is expected to result in a rigid shift of the cohesive energies, with the relative energy difference remaining unchanged. Moreover, the approximation with respect to the LT unit cell may even undererstimate the energy difference between the polymorphs, as discussed in Section 4.4. Therefore we conclude that the LT phase is energetically more stable. This is in agreement with experimental results.

5.2 Electronic Properties of HT and LT Sexithiophene

In Fig. 5.2, the band structures of HT and LT sexithiophene are shown. The directions of high symmetry chosen for the **k**-point path are illustrated in Fig. 5.3. The subbands corresponding to the uppermost valence-band (VB) pair and lowest conduction-band (CB) pair are highlighted in red Fig. 5.2.

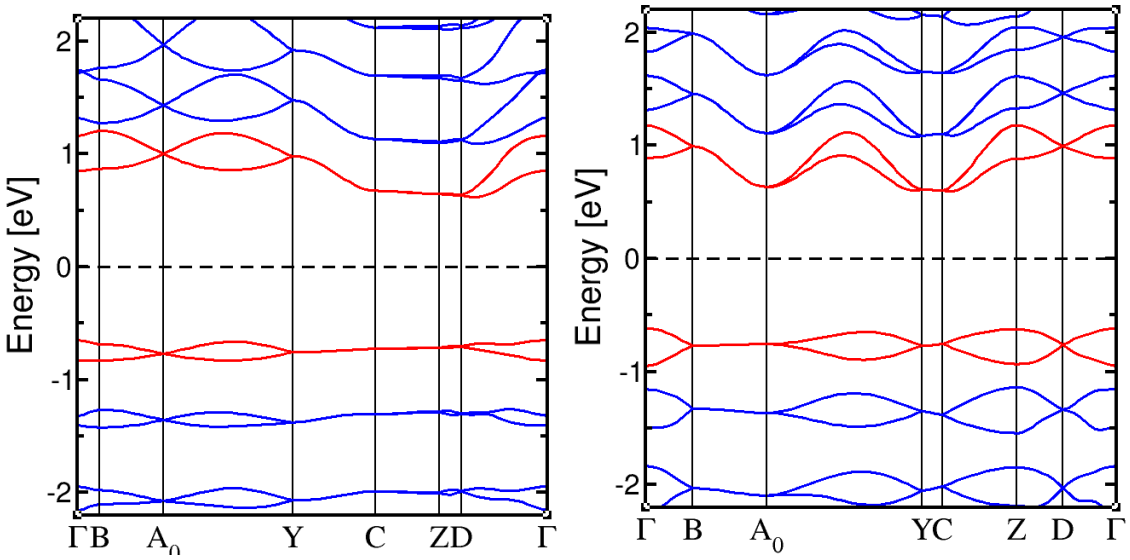

(a) LTr (b) HT

Figure 5.2: Band structures of the HT and LTr phases. The Fermi level is set to 0 eV and is indicated by a dashed line. The subbands closest du the Fermi level are shown in red.

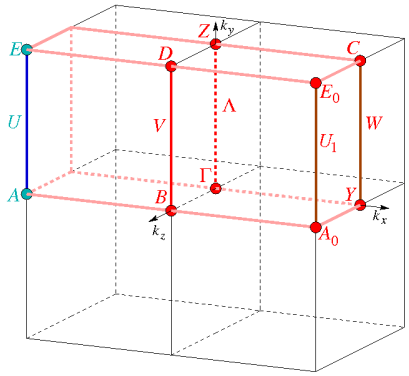

Figure 5.3: Brillouin zone of the HT and LTr structures. The high-symmetry points in units of $(2\pi/a, 2\pi/b, 2\pi/c)$ are $\Gamma = (0,0,0)$, $B = (1/2,0,0)$, $A_0 = (1/2,1/2,0)$, $Y = (0,1/2,0)$, $C = (0,1/2,1/2)$, $Z = (0,0,1/2)$ and $D = (1/2,0,1/2)$. Figure taken from Ref. [43].

Looking at the band structure of the two phase we notice very low dispersion. In the case of the LTr phase, the bandwidth of the VB is $W_{VB}^{LTr} = 0.2$ eV, while the bandwidth of the CB is larger, but still small, with $W_{CB}^{LTr} = 0.5$ eV. Due to the symmetry of the cell the bands are degenerate going from Y to C, and exhibit a small splitting from C to Z. The splitting is largest at the Γ-point and halfway inbetween the points A_0 and Y. Both HT and LT have indirect band gaps. The Kohn-Sham gaps are 1.2 eV and 1.1 for LTr and HT, respectively.

In the HT phase, the bandwidth is twice as large for the VB ($W_{VB}^{HT} = 0.4$), compared to the other phase, and a slightly larger for the CB ($W_{CB}^{HT} = 0.6$). The largest splitting is found at the points Γ and Z as well as halfway inbetween the points A_0 and Y. In addition to the degeneracy between Y and C, there is also a degeneracy between B and A_0.

6 Transition State

In this chapter we briefly review some of the most common approaches for finding transition paths. Difficulties of the methods, that are likely to arise in the context of this work, are pointed out. Finally, we describe our suggested transition path in detail.

6.1 Overview of Common Approaches

An important issue when studying growth mechanisms of organic crystals concerns the problem of finding the lowest energy pathway that rearranges the atoms from one stable structure to another. Such a minimum energy path (MEP) is critical for the estimation of transition rates, because the potential energy maximum along the MEP gives the activation energy barrier for the transition. A variety of methods have been proposed to solve the issue of finding the correct path and in particular the energy barrier [44]. We will now present a brief overview of some of the most commonly used methods.

One can start with an initial structure that corresponds to a potential energy minimum and follow a path of *slowest ascent* in a stepwise fashion. However, such a path might miss the saddle point which gives the transition barrier [45]. Another approach is the use of the *local harmonic approximation* for the potential energy surface. However, this involves diagonalizing the Hessian matrix of the potential energy and is not suited for DFT calculations where the second derivatives are not readily available [45]. Another common approach is the *nudged elastic band method*, which applies to problems where both the initial and the final structure are known [45]. From the known structures a number of intermediate structures along the reaction path are constructed. Each intermediate structure finds the lowest possible energy under the constraint that the structures must have equal spacing along the reaction path. This conditition is enforced by adding spring forces. This method looks promising because both the HT and LT structures of sexithiophene are available and this approach avoids the pitfalls of the other methods stated above. However, with the NEB, the transition states are based on linearly interpolated atomic positions. In the case of crystals with molecular constituents like sexithiophene this is not applicable, since it does not necessarily preserve the intramolecular bond lengths and angles. This would lead to unphysical results, since forces within a molecule are much stronger than forces between molecules. For instance, the bond energies occuring in sexithiophene are in the range of 3-4 eV [46], which is an order of magnitude larger than the energies of van der Waals interaction [5].

In the transition path of an organic crystal molecules should keep their shape and basically reorient themselves with respect to each other, with the unit cell changing

accordingly. The closest analogue to the method employed in this thesis is the *drag method* [47], which involves the construction of intermediate states, usually by linear interpolation of n degrees of freedom and relaxation of the remaining degrees of freedom. While conceptually simple, this method is not without problems. The transition path may depend on the choice of the parameters that are interpolated. Furthermore, upon relaxation, the parameters may "slip" near the saddle point, thereby giving a bad estimate for the energy barrier [48, 49].

Now that the relevant concepts have been introduced we will describe how to construct the transition path and will discuss potential issues that can arise.

6.2 Construction of the Transition Path

In the previous section we have seen a number of problems one may encounter with the different schemes. For this reason, we decided to construct the path manually, following the *drag* method.

We construct a transition path, that keeps the atomic positions of the molecules fixed and linearly interpolates the orientation of the molecules with respect to each other (herringbone angle, see Fig. 6.1a) and with respect to the unit cell (tilt angle, see Fig. 6.1b).

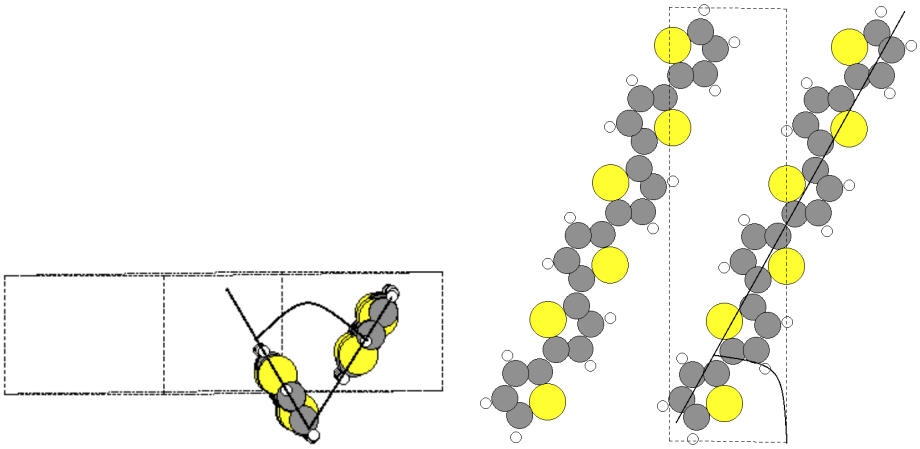

(a) Herringbone angle τ (b) Tilt angle ϕ

Figure 6.1: Angles governing the orientation of the molecules. The orientation of the molecules with respect to each other is given by the herringbone angle τ, while the tilt angle ϕ indicates the orientation with respect to the unit cell.

The unit cell itself has to be interpolated as well. This poses a potential problem, immediately. Rotations in three dimensional space do not generally commute and therefore the order of the rotations matters. Fortunately, the rotations in this case do commute, since

a change in the herringbone angle involves a rotation of neighbouring molecules with respect to each other, whereas the tilt angle governs the orientation of all molecules with respect to the unit cell. Therefore, we have both an "internal" rotation of the molecules with respect to each other and an "external" rotation that involves both molecules as a unit. Heuristically, this can be illustrated with the example of a passenger in a car. If the car does a left turn and the passenger looks to the floor the final position is the same, regardless of the order of rotations. In this case the head movement would correspond to the "internal" rotation and the car turning to the left would be the "external" rotation. This interchangeability of the order of rotations is not limited to orthogonal axes, as one might intuitively suspect. Instead, it is due to the fact that the "external" rotation does not change the axes that govern the "internal" rotation.

The guiding principle we adopt for constructing a realistic transition path is to make the smallest possible adjustments that transform the structures into each other. This does not guarantee that the resulting path will indeed be a MEP, but it provides an upper bound to the energetic transition barrier.

If we look at the unit cell parameters of the HT and LT phases (see Tab. 1.1) it seems that large changes are required in the modulus of the a and c axes. To overcome this

	HT	LTr
a' [Å]	20.67	22.35
b' [Å]	9.14	7.85
c' [Å]	5.68	6.03
β' [°]	97.78	90.8
τ' [°]	55	66
ϕ' [°]	41.5	23.5

Table 6.1: Relabeled unit cell parameters of the HT and LTr phases. Both phases have a monoclinic angle β'. τ' is the herringbone angle and ϕ' is the tilt angle.

problem we rotate the HT unit cell in order to minimize the seeming differences between the unit cells of the two polymorphs. Tab. 6.1 illustrates this change. The prime symbol is used to denote the parameters of the rotated HT unit cell, while for the LTr phase the primed and unprimed parameters are the same. The rotation of the HT unit cell constitutes a change of labels and does not affect the crystal structure itself, since there is no unique axis. As a result of the rotation, only small changes in the unit cell are required and therefore the volume stays approximately constant throughout the transformation. In fact, the largest variation of the volume is around 2%, which is comparable to the 1% difference in volume between the HT and LTr unit cells. However, one has to ensure that the replicas in the neighbouring cells are positioned correctly.

Taking these considerations into account, the transition path is constructed in three steps:

- The HT cell is rotated.
- The molecules are "frozen", i.e. intramolecular distances are kept fixed.
- The lattice constants, as well as the tilt and herringbone angles, are linearly interpolated.

Four intermediate states (1*o*4, 2*o*4, 3*o*4 and 4*o*4) are constructed, as depicted in Fig. 6.2. Tab. 6.2 shows the lattice parameters for each structure. The largest variation is with respect to the tilt angle ϕ', while the other parameters undergo small changes, only.

To define a reaction coordinate for our transition path we combine the parameters in Tab. 6.2 into a vector Φ. The lattice constants a', b', and c' vary *exactly* linearly upon optimization. The herringbone angle τ' and the tilt angle ϕ' are also linearly interpolated, but change while minimizing the forces that act on the atoms. Nevertheless, the angles change at most by 1°. Stricly speaking, the angles are not exactly linearly interpolated after the optimization, but the changes are sufficiently small to allow for the inclusion of both angles in the reaction coordinate Φ.

	HT	1o4	2o4	3o4	4o4	LTr
a' [Å]	20.67	21.01	21.34	21.68	22.02	22.35
b' [Å]	9.14	8.88	8.62	8.37	8.11	7.85
c' [Å]	5.68	5.75	5.82	5.89	5.96	6.03
τ' [°]	55.0	57.2	59.4	61.6	63.8	66.0
ϕ' [°]	41.5	37.9	34.3	30.7	27.1	23.5

Table 6.2: Unit cell parameters of the two phases and the transition structures. τ' is the herringbone angle and ϕ' is the tilt angle.

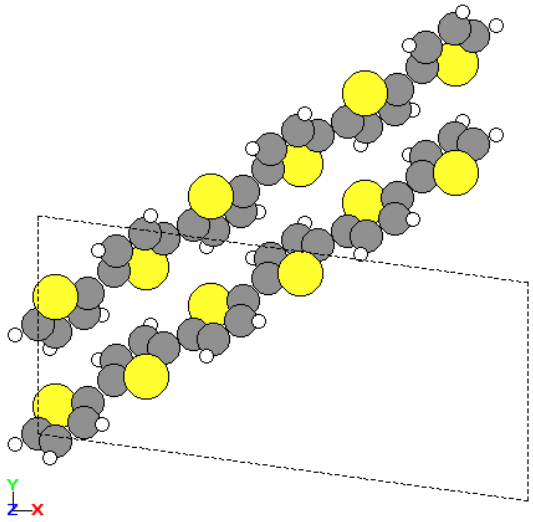

(a) HT

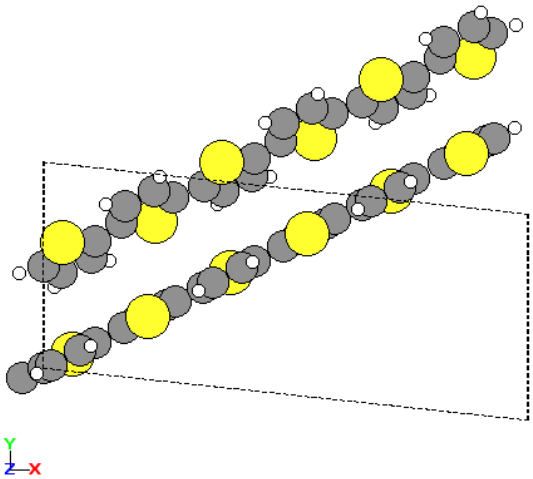

(b) 1o4

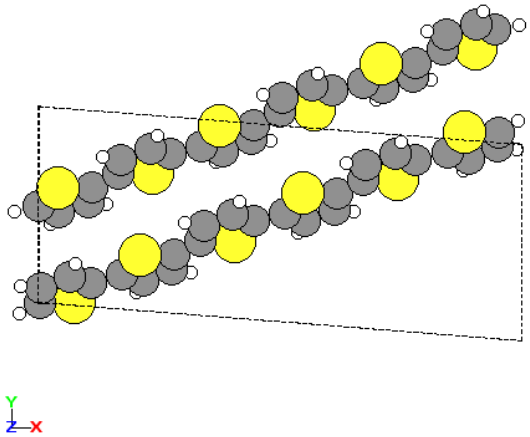

(c) 2o4

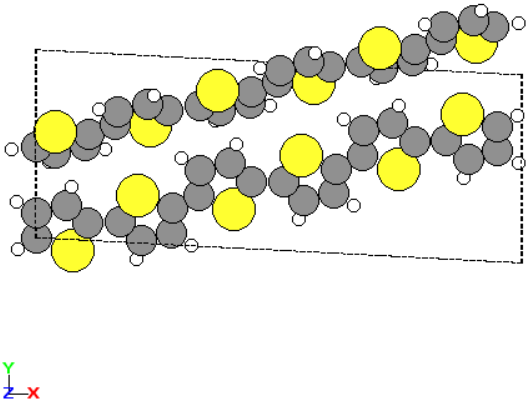

(d) 3o4

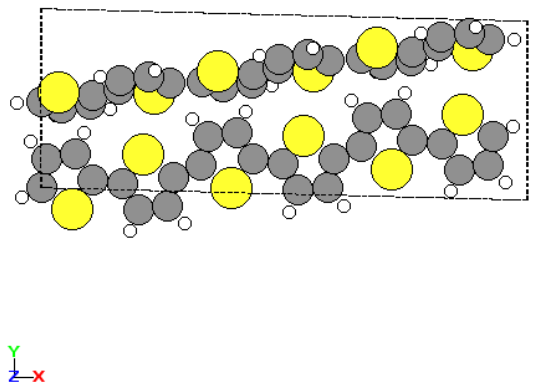

(e) 4o4

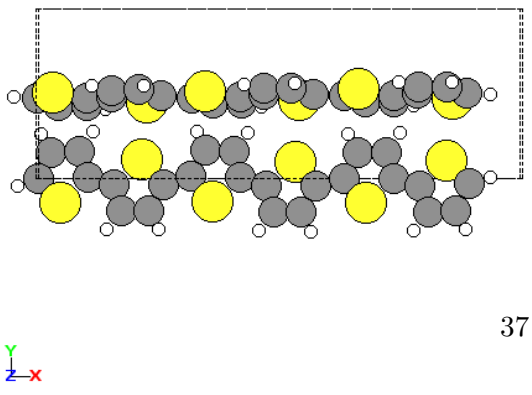

(f) LTr

Figure 6.2: Transition structures

7 Results II: Transition Barrier

In this chapter, we discuss the energy barrier between the HT and LTr phases, the effect of geometry optimization, and the electronic properties of the intermediate structures. Following the procedure presented in Chapters 4 and 6, the transition path is constructed, and the atomic positions are optimized by minimizing the forces acting on them. The "unrelaxed path" is shown in Fig. 7.1 and Tab. 7.1, while Fig. 7.2 and Tab. 7.2 contain the results after the structures have been relaxed.

Structure	E_{mol} [eV]	ΔE [eV]
HT	-89895.906	0.199
1o4	-89888.712	7.393
2o4	89890.254	5.851
3o4	-89885.973	10.131
4o4	-89885.565	10.540
LTr	-89896.105	0.000

Table 7.1: Total energy per molecule E_{mol} prior to minimizing the forces. ΔE is the energy difference with respect to the LTr structure.

Structure	E_{mol} [eV]	ΔE [meV]
HT	-89896.749	36
1o4	-89896.743	42
2o4	-89896.189	597
3o4	-89896.187	601
4o4	-89896.771	17
LTr	-89896.785	0

Table 7.2: Total energy per molecule E_{mol} after structure optimization. ΔE is the energy difference with respect to the LTr phase.

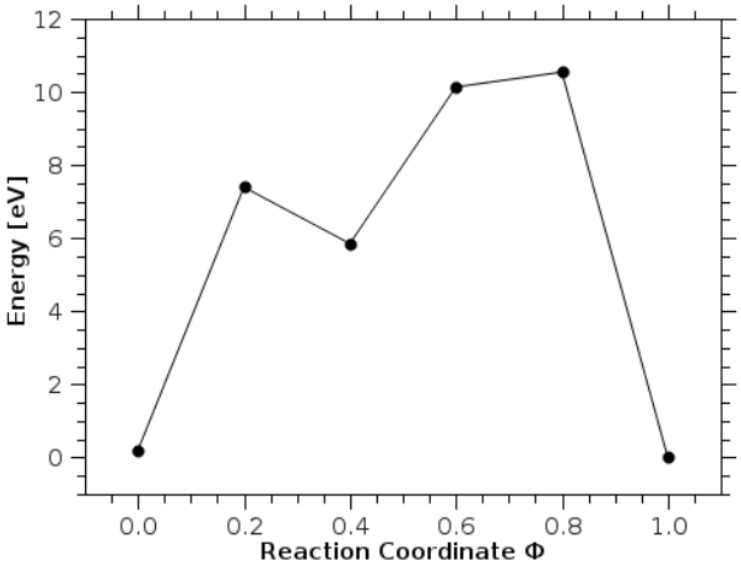

Figure 7.1: Transition barrier prior to structure relaxation showing the total energy per molecule for each structure. $\Phi = 0.0$ corresponds to the HT phase, while $\Phi = 1.0$ corresponds to the LTr phase. The energy corresponding to $\Phi = 1.0$ is set to 0 eV.

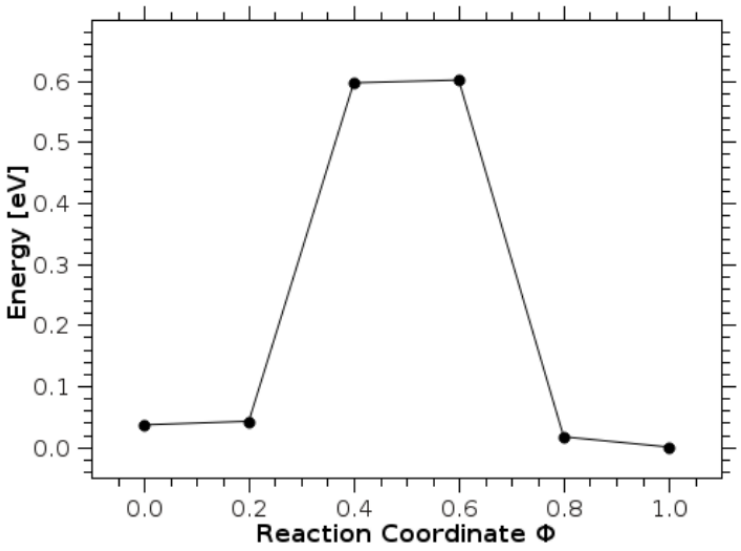

Figure 7.2: Transition barrier after structure relaxation showing the total energy per molecule for each structure. $\Phi = 0.0$ corresponds to the HT phase, while $\Phi = 1.0$ corresponds to the LTr phase. The energy corresponding to $\Phi = 1.0$ is set to 0 eV.

We begin with the unrelaxed barrier (Fig. 7.1). The HT phase, corresponding to $\Phi = 0.0$ as well as the LTr phase ($\Phi = 1.0$) are at the ends of the barrier. The activation energy per molecule is about 10.5 eV. The reason for this overly large barrier is that the transition states are far from their optimized geometries, while the HT and LTr phases are based on experimental data and therefore much closer to the relaxed configurations. The structures 1*o*4 and 4*o*4 are considerably higher in energy than the two known polymorphs.

To arrive at a realistic transition barrier, it is mandatory to have well optimized structures. This is clearly illustrated if we compare Figs. 7.1 and 7.2. After we have minimized the forces that act on the atoms, the energy landscape changes drastically. While the 4*o*4 structure at $\Phi = 0.8$ has the highest energy in the unrelaxed situation, in the relaxed case it has almost the same energy as the LTr phase. Similarly, the 1*o*4 structure at $\Phi = 0.2$ is very close to the energy of the HT phase. Both phases are similar in energy to their neighbouring structures, with energy differences of less than 20 meV (see also Tab. 7.2). Most importantly, the energy scale is one order of magnitude smaller than for the unrelaxed path. Upon relaxation the activation energy per molecule is about 0.6 eV. Similar barriers were found for another organic crystal [50]. The transition state 3*o*4 ($\Phi = 0.6$) is highest in energy, although the 2*o*4 state is only 4 meV lower in energy.

As part of the considerations in Chapter 6 it was mentioned that the intramolecular configuration are expected to remain unchanged during the transition, because the covalent bonds are much stronger than the vdW interaction between molecules. This can also be seen if we compare the bond lengths before and after structure optimization. The change in bond lengths is on the order of $\mathcal{O}(10^{-3}\mathring{A})$. A measure of the molecular arrangement along the long molecule axis is the distance between the two outermost sulfur atoms of each molecule. Here, the change due to structure optimization is on the order of $\mathcal{O}(10^{-2}\mathring{A})$. The distance increases slightly for the 1o4 and 4o4 states upon relaxation. For the 3o4 structure, the molecules are slightly quenched along the long molecule axis, which is plausible given that this state is close to the saddle point.

7.1 Electronic Properties of the Transition States

We now turn our attention to the band structures of the transition states.

It is worth mentioning that the transition structures belong to the $P1$ space group. Therefore, they exhibit only trivial symmetry. For this reason the **k**-point path is not the same as for the HT and LTr phase. To determine a **k**-point path we consider the space group for empty lattices, i.e. without the atoms ($P\bar{1}$). This leaves us with a slightly more symmetric Brillouin zone, as shown in Fig. 7.3.

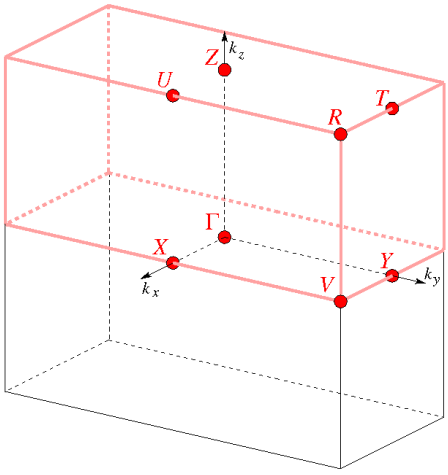

Figure 7.3: Brillouin zone of the transition state for *empty lattices*. Otherwise only the Γ-point remains. The high-symmetry points in units of $(2\pi/a,\ 2\pi/b,\ 2\pi/c)$ are $X = (1/2, 0, 0)$, $\Gamma = (0, 0, 0)$, $V = (1/2, 1/2, 0)$, $Y = (0, 1/2, 0)$, $Z = (0, 0, 1/2)$, $U = (1/2, 0, 1/2)$, $T = (0, 1/2, 1/2)$ and $R = (1/2, 1/2, 1/2)$. Figure taken from Ref. [43].

We choose the band structures of the 1*o*4, 3*o*4 and 4*o*4 transition states, because they are part of the plateaus that include the polymorphs (1*o*4 and 4*o*4) and present the apex of the barrier (3*o*4). The corresponding band structures are shown in Fig. 7.4. As before, in the case of the HT and LTr phases, all gaps are indirect ones. The Kohn-Sham gaps are 1.0 eV (1*o*5), 0.9 eV (3*o*5), and 1.2 eV (4*o*4). These are comparable to the Kohn-Sham gaps for the HT (1.1 eV) and LTr (1.2 eV) phases. All three band structures present a larger band splitting at the Γ-point, although in the 3*o*4 structure it is largest at point R in the VB and at point V in the CB. These are also the points that are expected to exhibit the largest charge carrier mobilities, due to the curvature. Away from these points the VBs are remarkably flat, especially for the 3*o*4 and 4*o*4 states. This implies high effective carrier masses and therefore low charge carrier mobilities in these regions. The bandwidths in the VBs decrease from 0.4 eV for the 1*o*4 and 3*o*4 states to 0.2 eV for the 4*o*4 state. In other words, the bandwidths in the VB are the same for the 1*o*4 state and the HT phase, as well as the 4*o*4 state and the LTr phase. In the CB the bandwidths tend to be larger with values of $W_{CB}^{1o4} = 0.6$ eV, $W_{CB}^{3o4} = 0.7$ eV and $W_{CB}^{4o4} = 0.7$ eV. Therefore, the bandwidths of the 1*o*4 and 4*o*4 states is 0.1 eV larger than those of the HT and LTr phase, respectively. The 1*o*4 and 4*o*4 structures are non-degenerate along V to Y, Z to U and T to Z to R.

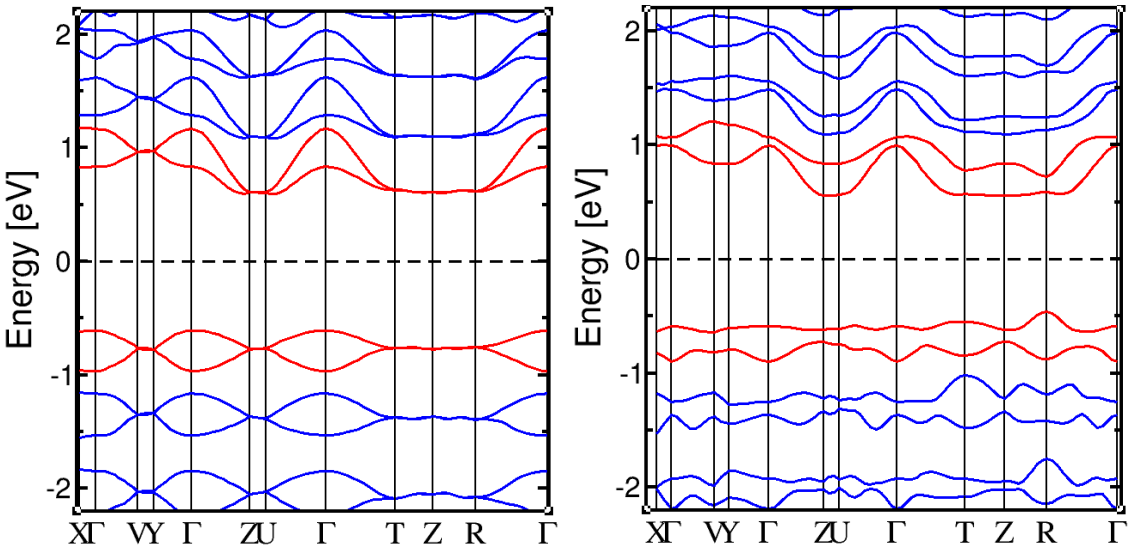

(a) 1o4

(b) 3o4

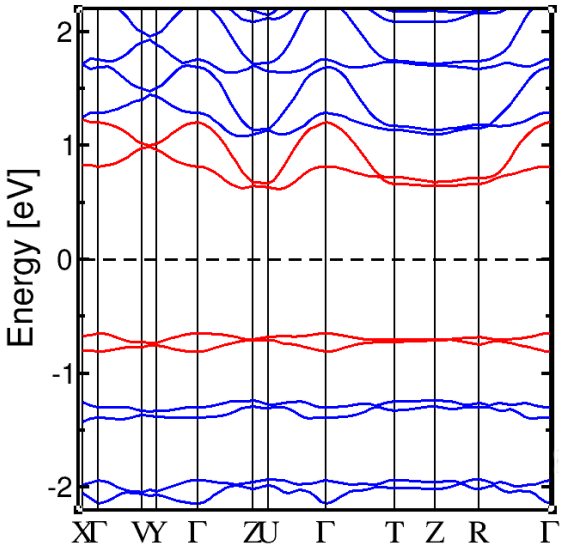

(c) 4o4

Figure 7.4: Band structures of the transition states 1o4, 3o4 and 4o4. The Fermi level is indicated by the dashed line. The subbands closest du the Fermi level are shown in red.

8 Conclusion and Outlook

In this work, we have presented an *ab initio* study of the HT and LT polymorphs of α-sexithiophene. In agreement with experimental observation [14], we have found the LT phase to be more stable than the HT phase, with an energy difference of 36.5 meV per molecule. To estimate the transition barrier between the two polymorphs a transition path was constructed, based on linear interpolation of the lattice constants, as well as the herringbone and tilt angles. After minimizing the forces acting on the atoms, we have found activation energies per molecule of 565 meV for the transition from HT to LT and 601 meV for the reverse transition.

There are many ways to build upon and extend this work. The transition path proposed in this work presents one of many possibilities and therefore a wide range of different reaction coordinates is conceivable. For instance, one could choose a different combination of parameters to define a reaction coordinate or vary the parameters that are included in our reaction coordinate Φ one by one. This will potentially result in different barrier heights.

Different functionals will be employed in place of LDA. An accurate treatment of vdW forces is particularly important and can be done as a post-processing on top of (semi-)local XC functionals using the vdW-DF. We will pursue this approach to test our expectation that the here obtained barrier height will stay the same.

Notation and Abbreviations

1o4, 2o4, 3o4, 4o4	intermediary transition states
6T	sexithiophene
α	atomic index or α-isomer characterized by coplanar rings
γ	scaling factor
Δ	Laplace operator
ϵ	eigenvalue of the Kohn-Sham equation
ϵ_{xc}	exchange-correlation energy per particle
ϵ_x	exchange energy per particle
ϵ_c	correlation energy per particle
λ	coupling constant
ϕ	Kohn-Sham wave function; tilt angle
φ	wave function of the basis set to represent ϕ
Φ	reaction coordinate
ψ	N-particle wave function
APW	augmented planewave basis
APW+lo	APW with local orbitals
CB	conduction-band
DFT	density functional theory
DOS	density of state
E[n]	ground state energy as a functional of the electron density
$F_{xc}(r_s)$	enhancement factor over LDA-exchange
$\mathbf{G}$	reciprocal lattice vector
G_{max}	planewave cutoff
$\hat{H}$	Hamiltonian
HT	high-temperature
I	interstitial region
$\mathbf{k}$	wave vector
k_F	modulus of the Fermi wave vector
KS	Kohn-Sham
l	angular momentum
LAPW	linearized augmented planewave basis
LAPW+LO	LAPW with local orbitals
LDA	local-density approximation
LT	low-temperature
LTr	reduced LT cell
M_α	mass of nucleus α
MEP	minimum energy path
MT	muffin-tin

N	number of electrons
n	principle quantum number
$n(\mathbf{r})$	electron density
n_{xc}^{λ}	exchange-correlation hole
$\overline{n}_{xc}$	coupling-constant averaged exchange-correlation hole
$\mathbf{r}$	position vector
`rgkmax`	`rgkmax`= $R_{MT}^{min}\ G_{max}$
R_{MT}	muffin-tin radius
r_s	Wigner-Seitz radius; a measure of the density
$\hat{T}$	operator of the kinetic energy
T_0	kinetic energy of a system of independent particles
u	overall uncertainty of the results
$\hat{U}$	operator of the electron-electron interaction
$u_{l\alpha}(r_\alpha)$	solution of the radial Schrödinger equation
$\hat{V}$	operator of the external potential
$\hat{V}_{KS}$	operator of the Kohn-Sham potential
v	single-particle external potential
v_H	single-particle Hartree potential
v_{KS}	single-particle Kohn-Sham potential
v_{xc}	single-particle exchange-correlation potential
VB	valence-band
vdW	van der Waals
vdW-DF	van der Waals density functional
W	bandwith
xc	exchange-correlation
$Y_{lm}(\hat{\mathbf{r}})$	spherical harmonics

Bibliography

[1] S. R. Forrest, "The road to high efficiency organic light emitting devices," *Organic Electronics*, vol. 4, pp. 45–48, Sept. 2003.

[2] S. R. Forrest, "The path to ubiquitous and low-cost organic electronic appliances on plastic," *Nature*, vol. 428, pp. 911–918, Apr. 2004.

[3] P. Peumans, A. Yakimov, and S. R. Forrest, "Small molecular weight organic thin-film photodetectors and solar cells," *Journal of Applied Physics*, vol. 93, pp. 3693–3723, Apr. 2003.

[4] M. Muccini, "A bright future for organic field-effect transistors," *Nature Materials*, vol. 5, pp. 605–613, Aug. 2006.

[5] J. Fraxedas, *Molecular Organic Materials: From Molecules to Crystalline Solids*. Cambridge University Press, Apr. 2006.

[6] S. L. Price, "Predicting crystal structures of organic compounds," *Chemical Society Reviews*, vol. 43, pp. 2098–2111, Mar. 2014.

[7] D. A. Bardwell, C. S. Adjiman, Y. A. Arnautova, E. Bartashevich, S. X. M. Boerrigter, D. E. Braun, A. J. Cruz-Cabeza, G. M. Day, R. G. Della Valle, G. R. Desiraju, B. P. van Eijck, J. C. Facelli, M. B. Ferraro, D. Grillo, M. Habgood, D. W. M. Hofmann, F. Hofmann, K. V. J. Jose, P. G. Karamertzanis, A. V. Kazantsev, J. Kendrick, L. N. Kuleshova, F. J. J. Leusen, A. V. Maleev, A. J. Misquitta, S. Mohamed, R. J. Needs, M. A. Neumann, D. Nikylov, A. M. Orendt, R. Pal, C. C. Pantelides, C. J. Pickard, L. S. Price, S. L. Price, H. A. Scheraga, J. van de Streek, T. S. Thakur, S. Tiwari, E. Venuti, and I. K. Zhitkov, "Towards crystal structure prediction of complex organic compounds – a report on the fifth blind test," *Acta Crystallographica Section B Structural Science*, vol. 67, pp. 535–551, Dec. 2011.

[8] A. Gavezzotti, "Are crystal structures predictable?," *Accounts of Chemical Research*, vol. 27, no. 10, pp. 309–314, 1994.

[9] D. Fichou, *Handbook of Oligo- and Polythiophenes*. John Wiley & Sons, Nov. 2008.

[10] A. Tsumura, H. Koezuka, and T. Ando, "Polythiophene field-effect transistor: Its characteristics and operation mechanism," *Synthetic Metals*, vol. 25, pp. 11–23, July 1988.

[11] G. Horowitz, R. Hajlaoui, and F. Kouki, "An analytical model for the organic field-effect transistor in the depletion mode. Application to sexithiophene films and single crystals," *The European Physical Journal - Applied Physics*, vol. 1, pp. 361–367, Mar. 1998.

[12] T. Siegrist, R. Fleming, R. Haddon, R. Laudise, A. Lovinger, H. Katz, P. Bridenbaugh, and D. Davis, "The crystal structure of the high-temperature polymorph of α–hexathienyl (α–6t/HT)mc," *Journal of Materials Research*, vol. 10, no. 09, pp. 2170–2173, 1995.

[13] G. Horowitz, B. Bachet, A. Yassar, P. Lang, F. Demanze, J.-L. Fave, and F. Garnier, "Growth and characterization of sexithiophene single crystals," *Chemistry of Materials*, vol. 7, no. 7, pp. 1337–1341, 1995.

[14] L. Pithan, C. Cocchi, H. Zschiesche, C. Weber, A. Zykov, S. Bommel, S. J. Leake, P. Schäfer, C. Draxl, and S. Kowarik, "Light Controls Polymorphism in Thin Films of Sexithiophene," *Crystal Growth & Design*, Jan. 2015.

[15] R. G. Della Valle, E. Venuti, A. Brillante, and A. Girlando, "Are crystal polymorphs predictable? The case of sexithiophene," *The Journal of Physical Chemistry A*, vol. 112, no. 29, pp. 6715–6722, 2008.

[16] K. Burke, "The ABC of DFT." http://www.chem.uci.edu/∼kieron/dftold2/materials/bookABCDFT/gamma/g1.pdf.

[17] R. M. Dreizler and E. K. U. Gross, *Density Functional Theory*. Springer, 1990.

[18] E. Engel and R. M. Dreizler, *Density Functional Theory*. Theoretical and Mathematical Physics, Berlin, Heidelberg: Springer Berlin Heidelberg, 2011.

[19] C. Fiolhais, F. Nogueira, and M. A. L. Marques, *A Primer in Density Functional Theory*. Springer Science & Business Media, June 2003.

[20] L. H. Thomas, "The calculation of atomic fields," *Mathematical Proceedings of the Cambridge Philosophical Society*, vol. 23, pp. 542–548, Jan. 1927.

[21] E. Fermi, "Eine statistische Methode zur Bestimmung einiger Eigenschaften des Atoms und ihre Anwendung auf die Theorie des periodischen Systems der Elemente," *Zeitschrift für Physik*, vol. 48, pp. 73–79, Jan. 1928.

[22] P. Hohenberg and W. Kohn, "Inhomogeneous electron gas," *Physical Review*, vol. 136, pp. B864–B871, Nov. 1964.

[23] M. Levy, "Electron densities in search of hamiltonians," *Physical Review A*, vol. 26, pp. 1200–1208, Sept. 1982.

[24] W. Kohn and L. J. Sham, "Self-consistent equations including exchange and correlation effects," *Physical Review*, vol. 140, pp. A1133–A1138, Nov. 1965.

[25] E. Teller, "On the Stability of Molecules in the Thomas-Fermi Theory," *Reviews of Modern Physics*, vol. 34, pp. 627–631, Oct. 1962.

[26] J. P. Perdew, K. Burke, and M. Ernzerhof, "Generalized gradient approximation made simple," *Physical Review Letters*, vol. 77, pp. 3865–3868, Oct. 1996.

[27] J. Tao, J. P. Perdew, V. N. Staroverov, and G. E. Scuseria, "Climbing the density functional ladder: Nonempirical meta-generalized gradient approximation designed for molecules and solids," *Physical Review Letters*, vol. 91, p. 146401, Sept. 2003.

[28] C. Adamo and V. Barone, "Toward reliable density functional methods without adjustable parameters: The PBE0 model," *The Journal of Chemical Physics*, vol. 110, pp. 6158–6170, Apr. 1999.

[29] X. Ren, P. Rinke, C. Joas, and M. Scheffler, "Random-phase approximation and its applications in computational chemistry and materials science," *Journal of Materials Science*, vol. 47, pp. 7447–7471, Nov. 2012.

[30] R. O. Jones and O. Gunnarsson, "The density functional formalism, its applications and prospects," *Reviews of Modern Physics*, vol. 61, pp. 689–746, July 1989.

[31] E. Wigner, "On the interaction of electrons in metals," *Physical Review*, vol. 46, pp. 1002–1011, Dec. 1934.

[32] D. M. Ceperley and B. J. Alder, "Ground state of the electron gas by a stochastic method," *Physical Review Letters*, vol. 45, pp. 566–569, Aug. 1980.

[33] E. H. Lieb and S. Oxford, "Improved lower bound on the indirect coulomb energy," *International Journal of Quantum Chemistry*, vol. 19, no. 3, pp. 427–439, 1981.

[34] A. Gulans, S. Kontur, C. Meisenbichler, D. Nabok, P. Pavone, S. Rigamonti, S. Sagmeister, U. Werner, and C. Draxl, "exciting: a full-potential all-electron package implementing density-functional theory and many-body perturbation theory," *Journal of Physics: Condensed Matter*, vol. 26, p. 363202, Sept. 2014.

[35] O. K. Andersen, "Linear methods in band theory," *Physical Review B*, vol. 12, pp. 3060–3083, Oct. 1975.

[36] E. Sjöstedt, L. Nordström, and D. J. Singh, "An alternative way of linearizing the augmented plane-wave method," *Solid State Communications*, vol. 114, pp. 15–20, Mar. 2000.

[37] http://exciting-code.org/.

[38] R. Byrd, P. Lu, J. Nocedal, and C. Zhu, "A Limited Memory Algorithm for Bound Constrained Optimization," *SIAM Journal on Scientific Computing*, vol. 16, pp. 1190–1208, Sept. 1995.

[39] P. Ranzieri, A. Girlando, S. Tavazzi, M. Campione, L. Raimondo, I. Bilotti, A. Brillante, R. G. Della Valle, and E. Venuti, "Polymorphism and phonon dynamics of α-quaterthiophene," *ChemPhysChem*, vol. 10, no. 4, pp. 657–663, 2009.

[40] www.chemspider.com/Chemical-Structure.9515841.html.

[41] D. Nabok, P. Puschnig, and C. Ambrosch-Draxl, "Cohesive and surface energies of π-conjugated organic molecular crystals: A first-principles study," *Physical Review B*, vol. 77, p. 245316, June 2008.

[42] K. Hummer, P. Puschnig, and C. Ambrosch-Draxl, "\textit{Ab initio} study of anthracene under high pressure," *Physical Review B*, vol. 67, p. 184105, May 2003.

[43] http://www.cryst.ehu.es/.

[44] M. L. Mckee and M. Page, "Computing reaction pathways on molecular potential energy surfaces," in *Reviews in Computational Chemistry* (K. B. Lipkowitz and D. B. Boyd, eds.), pp. 35–65, John Wiley & Sons, Inc., 1993.

[45] D. Sheppard, P. Xiao, W. Chemelewski, D. D. Johnson, and G. Henkelman, "A generalized solid-state nudged elastic band method," *The Journal of Chemical Physics*, vol. 136, p. 074103, Feb. 2012.

[46] www.science.uwaterloo.ca/∼cchieh/cact/c120/bondel.html.

[47] G. Henkelman, G. Jóhannesson, and H. Jónsson, "Methods for Finding Saddle Points and Minimum Energy Paths," in *Theoretical Methods in Condensed Phase Chemistry* (S. D. Schwartz, ed.), no. 5 in Progress in Theoretical Chemistry and Physics, pp. 269–302, Springer Netherlands, 2002.

[48] M. J. Rothman and L. L. Lohr Jr., "Analysis of an energy minimization method for locating transition states on potential energy hypersurfaces," *Chemical Physics Letters*, vol. 70, pp. 405–409, Mar. 1980.

[49] T. A. Halgren and W. N. Lipscomb, "The synchronous-transit method for determining reaction pathways and locating molecular transition states," *Chemical Physics Letters*, vol. 49, pp. 225–232, July 1977.

[50] G. Hlawacek, P. Puschnig, P. Frank, A. Winkler, C. Ambrosch-Draxl, and C. Teichert, "Characterization of Step-Edge Barriers in Organic Thin-Film Growth," *Science*, vol. 321, pp. 108–111, July 2008.

Selbständigkeitserklärung

Ich erkläre hiermit, dass ich die vorliegende Arbeit selbständig verfasst und noch nicht für andere Prüfungen eingereicht habe. Sämtliche Quellen einschließlich Internetquellen, die unverändert oder abgewandelt wiedergegeben werden, insbesondere Quellen für Texte, Grafiken, Tabellen und Bilder, sind als solche kenntlich gemacht. Mir ist bekannt, dass bei Verstößen gegen diese Grundsätze ein Verfahren wegen Täuschungsversuchs bzw. Täuschung eingeleitet wird.

Berlin, den March 18, 2015 .....